IR 81-2338R

MHD MATERIALS - SEED/SLAG INTERACTIONS AND EFFECTS

QUARTERLY PROGRESS REPORT

April 1 - June 30, 1981

Samuel J. Schneider
Project Manager

Center for Materials Science
U. S. Department of Commerce
National Bureau of Standards
Washington, D. C. 20234

PREPARED FOR THE UNITED STATES
DEPARTMENT OF ENERGY
MHD OFFICE

"This report was prepared as an account of work sponsored by the United States Government. Neither the United States nor the United States Department of Energy, nor any of their employees, nor any of their contractors, subcontractors, or their employees, makes any warranty, expressed or implied, or assumes any legal liability or responsibility for the accuracy, completeness, or usefulness of any information, apparatus, product or process disclosed, or represents that its use would not infringe privately owned rights."

TABLE OF CONTENTS

		Page
I.	SUMMARY OF PROGRESS TO DATE.	1
II.	DETAILED DESCRIPTION OF TECHNICAL PROGRESS	2
	1. Thermochemistry of Seed and Slag	2
	2. Electrical Conductivity and Polarization	24
	3. Corrosion of Downstream MHD Components	30

I. Summary of Progress to Date

1. Thermochemistry of Seed and Slag

Development of a model equation based on four component simplified Western channel slags continued. Additional data were included to modify the constants previously obtained. The equation uses three linear terms in the concentration variables, a constant term, and a term in 1/T to relate log P_K to the concentration variables and temperature. The modified equation predicts changes in the K pressure of 16, 2, and -3 percent for increases in the concentration of K_2O, CaO, and Al_2O_3 of 1 percent, respectively. The model equation is found to predict K pressures within a factor of 2 of those measured for other more complicated slags if the Fe_2O_3 and MgO components are assumed to be chemically equivalent to Al_2O_3 and CaO, respectively. The model equation is less successful in predicting K pressures over slags containing less than 10 wt.% CaO or simpler slag solutions.

The formulation of a phase equilibrium derived K_2O-CaO-Al_2O_3-SiO_2 model for prediction of potassia activities has been presented.[2] This is largely an empirical model and has not been fully developed and tested. In a more theoretical effort, the quasichemical melt polymerization model is extended to calculation of liquidus surfaces in the system K_2O-CaO-Al_2O_3-SiO_2. The practical goal of this effort is an algorithm for prediction of slag melting behavior as a function of composition. So far the fit to six subsystems is reasonably good, but an independent test on a seventh points up the need for considerable refinement. The model allows consideration of polyatomic cations as well as polymeric anions.

2. Electrical Conductivity and Polarization

An average anode and cathode function has been calculated which shows that in a low-iron, high-calcia slag, there is considerable ionic conductivity above 1400 °C. SEM and EDAX coupled with previous XRD analyses show that iron-alumina spinel is the only detected conducting crystalline material but that bridging of this material through the main component (leucite or potash feldspar) is not sufficient to explain the observed conductivity below the slag solidification point.

3. Corrosion of Downstream Components

Specimens of NiCrAlY, $MgAl_2O_4$ (spinel) and ZrO_2 (doped with MgO) arc plasma sprayed on AISI 1015 steel were examined by SEM/EDX techniques for species distribution and structural integrity. Analysis was conducted on metallographically prepared specimens taken from sections of material in the as-received condition, after cycling in air to 700 °C and after cycling to 700 °C in forming gas. The ramp rate was approximately 3 °C/min. and the peak temperature was maintained for about 36 hours. Metallographically prepared sections of AISI 1015 steel tubing, the material used as a substrate for the arc plasma sprayed coatings, were analyzed also by SEM/EDX techniques after exposure to fuel rich and oxygen rich K_2SO_4 seeded hot gas streams. Tube wall temperature for these exposure tests was held at 590 °C. The extent and some aspects of the chemical nature of the reaction zone between the metal and the deposited salt coating was determined.

II. Detailed Description of Technical Progress

1. Thermochemistry of Seed and Slag (E. R. Plante and L. P. Cook)

A. Vaporization Studies (E. R. Plante)

An objective of the current work is to obtain K-pressure data for selected compositions of the four component system, K_2O-CaO-Al_2O_3-SiO_2. These selected compositions correspond to the channel slag which would be produced by the interaction of seeded combustion gases with simplified "Western" coal ash. A second objective is to predict the K-pressure or K_2O activity in melts with compositions not too different from those studied by using the data base generated to develop an initially empirical model. Finally, it is planned to extend the model to other coal ash compositions, including additional components, such as Fe_2O_3 and MgO. The basic use of such a model is to aid in determining the magnitude of seed loss to slag in MHD systems and to suggest the best method to minimize this effect.

Thus far, vapor pressure data have been determined for four different samples. Table 1 lists the initial mineral constituents and the starting and final composition in wt.% of each of the four components. All vapor pressure measurements have been obtained using a Knudsen effusion, modulated beam mass spectrometric method.

Table 1

Mineral Constituents and Composition of Vaporization Samples

Sample	Mineral Constituents (wt.%)	Initial/Final Composition wt.% K_2O	CaO	Al_2O_3	SiO_2
KCAS-VP-1	$KAlSiO_4$(49.8), Ca_2SiO_4(16.5)	14.8	27.5	22.2	35.5
	$Ca_2Al_2SiO_7$(16.5), $Ca_3Si_2O_7$(17.2)	1.6	31.8	25.7	40.9
KCAS-VP-2	$KAlSiO_4$(28.6), $KAlSi_2O_6$(13.8)	11.5	17.6	33.7	37.2
	$Ca_2Al_2SiO_7$(28.9), $CaAl_2Si_2O_8$(28.7)	6.1	18.7	35.7	39.5
KCAS-VP-3	$KAlSiO_4$(42.0), $CaSiO_3$(58.0)	12.5	28.0	13.5	46.0
		1.8	31.4	15.2	51.6
KCAS-VP-4	$KAlSiO_4$(66.9), Ca_2SiO_4(33.1)	19.9	21.6	21.6	37.0
		2.7	26.2	26.2	44.9

Progress: During this quarter analysis of the KCAS-VP-4 data was completed and comparison of the model results with experimental data from other more complicated slag compositions was made. As in previous measurements, the data were separated into groups to limit the change in the K_2O composition and least squares analysis of the data were made to determine the slope and intercept in the equation,

$$\log P_K = A/T + B.$$

These data are tabulated in Table 2 along with similar results obtained from results of the KCAS-VP-1, KCAS-VP-2, and KCAS-VP-3 series. The basic data in the four series of measurements includes 389 K pressures at varying T and compositions of K_2O, CaO, Al_2O_3, and SiO_2. The slope terms in Table 2 generally do not deviate greatly from -17000 ± 1000 except for the 3/13/80 and 3/14/80 experiments from the KCAS-VP-1 series and the 12/15/80 and 12/16/80 experiments from the KCAS-VP-4 series. These data were obtained at compositions at which the calculated K_2O concentrations were relatively high. The relatively high slopes could be explained by the presence of a crystalline $KAlSiO_4$ phase in the solution at lower temperatures which gradually dissolved as the temperature was increased leading to enhanced K_2O concentration at the higher temperatures. Slopes lower than 17,000 may be due to impurity evaporation (unreacted K_2CO_3) at the beginning of the series or to inclusion of too wide a K_2O composition in the data analyzed.

Because the variation of K_2O concentration is expected to have the greatest effect on the K pressure each set of data was also fit to the equation

$$\log P_K = A/T + B + C\ (\text{wt.\% } K_2O).$$

The results of this calculation are shown in Table 3. Again, the average slope is close to -17,000 ± 1000. The change in K pressure per percent change in K_2O concentration varies from a high of 22 percent to a low of 17 percent. Thus, the variation in K pressure is close to the same value for all four series.

In the previous quarterly report, data from the KCAS-VP-1, KCAS-VP-2, and KCAS-VP-3 data were used to determine coefficients for the equation

$$\log P_K(\text{atm}) = A/T + B + C(\text{wt.\% } K_2O) + D(\text{wt.\% CaO}) + E(\text{wt.\% } Al_2O_3).$$

Inclusion of the KCAS-VP-4 data in the data pool leads to slight changes in the coefficients. A comparison of the coefficients is given in Table 4. The first set of coefficients based on the KCAS-VP-1, 2, and 3 experiments indicates that each percent increase in the K_2O concentration increases the K pressure by 20 percent and each percent increase in the Al_2O_3 concentration decreases the K pressure by 4 percent. The effect of an increase of a percent in the CaO concentration is essentially negligible but leads to an increase in the K pressure of 0.4 percent. The second set of coefficients based on the inclusion also of the KCAS-VP-4 data shows an increase in the K pressure of 16 percent for each percent increase in the K_2O concentration, an increase of 2 percent for a percent increase in the CaO concentration and a 3 percent decrease in the K pressure for a percent increase in the Al_2O_3 concentration. The agreement of these model equations with each other is good but we will use that based on all of the experimental data rather than the first three series.

Table 2

Slope, Intercept, and Standard Deviations for K-Pressure Data

Expt. Id	Wt.% K_2O	A	SD,A	B	SD,B
KCAS-VP-1					
3/13/80	14.8-12.4	-20,047	391	8.062	.255
3/14/80	12.4- 9.3	-19,071	524	7.196	.334
3/18/80	9.3- 7.2	-17,429	452	5.976	.289
3/18/80	6.2- 4.8	-16,372	210	4.986	.129
3/21/80	4.8- 4.0	-16,896	279	5.207	.178
KCAS-VP-2					
5/14/80	11.4-10.7	-14,632	434	4.200	.278
5/15/80	10.7- 8.6	-16,366	180	5.097	.112
5/16/80	8.6- 6.5	-17,571	257	5.656	.158
5/19/80	6.5- 6.2	-16,606	526	4.992	.321
KCAS-VP-3					
8/13/80	12.5-10.8	-15,052	775	4.983	.512
8/14/80	10.8-10.3	-17,512	453	6.282	.298
8/14/80	10.3- 7.4	-15,441	612	4.732	.374
8/15/80	7.4- 6.0	-16,006	518	5.178	.362
8/15/80	6.0- 3.9	-15,390	320	4.544	.197
8/18/80	3.9- 3.2	-16,948	801	5.417	.505
KCAS-VP-4					
12/15/80	19.5-18.7	-18,153	893	6.994	.618
12/16/80	18.6-17.8	-19,616	423	7.978	.293
12/17/80	17.8-15.7	-17,611	308	6.457	.213
12/29/80	15.7-14.9	-16,375	722	5.588	.501
12/30/80	14.9-13.2	-17,620	204	6.392	.139
1/13/81	13.2-10.8	-17,740	285	6.301	.191
1/14/81	10.8- 6.8	-16,567	697	5.294	.457
1/15/81	6.8- 2.7	-14,906	720	3.938	.449

Table 3

Slope, Intercept, and K_2O Coefficient for KCAS-VP-Series

Series	A	SD,A	B	SD,B	C	SD,C
KCAS-VP-1	-17,940	326	5.491	.198	.0876	.0047
KCAS-VP-2	-16,528	241	4.412	.147	.0844	.0063
KCAS-VP-3	-15,811	283	4.405	.174	.0786	.0049
KCAS-VP-4	-17,445	190	5.248	.119	.0677	.0026

Table 4
Coefficients and Standard Deviations for Model Equation. First set of coefficients are for KCAS-VP-1, KCAS-VP-2, and KCAS-VP-3 data. Second set of coefficients includes KCAS-VP-4 data in addition.

Term	Value	Standard Deviation
A	-16,794	176
B	5.288	0.173
C	7.887E-2	0.309E-2
D	1.741E-3	0.318E-3
E	-1.825E-2	0.209E-2
A	-17,271	140
B	5.281	.172
C	6.516E-2	.236E-2
D	1.002E-2	.345E-2
E	-1.318E-2	.217E-2

Both model equations show a standard deviation in the fit of 35 percent while maximum deviations in individual points are less than 100 percent except for a relatively few cases.

Comparison with Slag Data: Some comparisons of the model equation with data obtained on more complicated slags as well as with simpler slags have been made. Because the model equation is based on data obtained for four component slags in which the slag phase is mainly liquid it would be expected to be better suited to predict the K pressure over slags which are primarily in the liquid state.

Figure 1 shows a plot of $(P_K^2 \cdot P_{O_2}^{\frac{1}{2}})^{0.4}$ over a synthetic slag (K2) having an initial composition of 47.3 wt.% SiO_2, 11.1 Al_2O_3, 12.0 Fe_2O_3, 13.9 CaO, 7.0 MgO, and 8.7 K_2O. This slag was specially formulated to have a low melting point and was pourable from a container at 1250 °C. The term $(P_K^2 \cdot P_{O_2}^{\frac{1}{2}})^{0.4}$ is equal to the K pressure which would be found if the O_2 pressure over the slag had not been effected by an enhanced O_2 pressure because of the presence of Fe_2O_3 in the slag. In order to use the model equation to compare the K pressure predicted with that measured we assume that Al_2O_3 and Fe_2O_3 are chemically similar and constitute 23.1 wt.% of the slag. Likewise, we assume that CaO and MgO are chemically alike and constitute 20.9 wt.% of the slag. Using these modifications, that is, a slag consisting of 47.3 wt.% SiO_2, 23.1 Al_2O_3, 20.9 CaO, and 8.7 K_2O, and the coefficients based on all four series of the KCAS data the resulting line predicted by the model is plotted in Figure 1. It can be seen that the agreement between the model line and the experimental points is extraordinarily good.

As a second test of the model a comparison with data for a Western model slag was made. Some of this data was previously reported by Plante and Cook (1). The initial composition of this slag was 34.7 wt.% SiO_2, 24.5 Al_2O_3, 5.5 Fe_2O_3, 9.3 CaO, 3.3 MgO, and 22.7 K_2O. Using the same approximations as previously, the data in Figure 2 covering the K_2O concentration range from 17.6 to 18.9 wt.% K_2O can be compared with an average slag concentration of 18.2 wt.% K_2O, 13.3 CaO, and 31.8 Al_2O_3 while the data shown in Figure 3 which covers the K_2O concentration range from 12.9 to 10.8 wt.% K_2O can be compared with the average slag composition 11.8 wt.% K_2O, 14.4 CaO, and 34.2 Al_2O_3. In the comparison of the model line in Figure 2 with the experimental data the greatest deviation occurs at the lower temperatures. This could result because of precipitation of $KAlSiO_4$ from the melt as the temperature is decreased. Cook (2) has made estimates of the K_2O concentration in the liquid phase for the Western slag composition. For the lowest temperature point in Figure 2 the K_2O concentration would be 17.6 wt.% if all the slag was in the liquid phase while Cook's data indicate that the K_2O concentration at this temperature (1530 K) would be only 11.7 wt.%; the remaining K_2O being present as $KAlSiO_4$(c). For this point the observed pressure is 3.4×10^{-6} atm while the model predicts a pressure of 7.5×10^{-6} atm. The difference between the actual K_2O concentration and that used in the model calculation is about 6.5 percent so that this difference alone would cause the calculated line at 1530 K to be high by 104 percent. This would appear to indicate that if the actual K_2O concentration in the slag solution were known, significantly better agreement between the observed pressure and the pressure predicted by the model would be found.

However, there is a significant increase in slope of the data obtained on lowering the temperature as compared to the data obtained when the temperature was increased. The slope obtained on lowering the temperature is more consistent with the precipitation of $KAlSiO_4$ from the melt suggesting that the data obtained when the temperature was increased may have been influenced by the evaporation of residual impurities (probably K_2CO_3) from the melt. The data shown in Figure 3 also shows quite reasonable agreement with the model prediction. This is quite surprising because the slope of the data in Figure 3 (-20,500) is much steeper than the model slope (-17,300). The agreement of the western slag data with the model equation is not significantly poorer than some of the data used to derive the model equation.

Comparison of the K pressure predicted by the model has also been made with a few other slag compositions. For low calcia slags the model predicts too high a K pressure by a factor of 5 to 10 or more. Further work on comparison with multicomponent (5 or more components) slags is in progress. Although the term in the model governing the K pressure dependence on the CaO concentration is not large, the presence of CaO in the slag solution at concentration in excess of 10 percent appears to be paramount to obtaining good agreement (within a factor of 2) between the measured K pressure over the slag and the K pressure predicted by the model.

Comparison of the predicted model pressure with K pressures of simple slag solutions such as K_2O-SiO_2 or compositions in the K_2O-SiO_2-Al_2O_3 system shows that the model pressure is always higher than the measured pressure by factors of 2 (best agreement at low K_2O concentration) to 10 or greater. Although the model based on the four component K_2O-CaO-Al_2O_3-SiO_2 slags would not be expected to apply to the simpler slags, the direction of disagreement probably indicates the importance of CaO in increasing the K pressure.

Plans: Continue comparison of K pressure predicted by four component model with those over other slag compositions. Supplement model data with data using lower CaO concentration.

References

1. E. R. Plante and L. P. Cook, Seventeenth Symposium on Engineering Aspects of Magnetohydrodynamics, Stanford, CA (1978).

2. L. P. Cook, Seventh International Conference on MHD Electrical Power Generation, Cambridge, MA (1980).

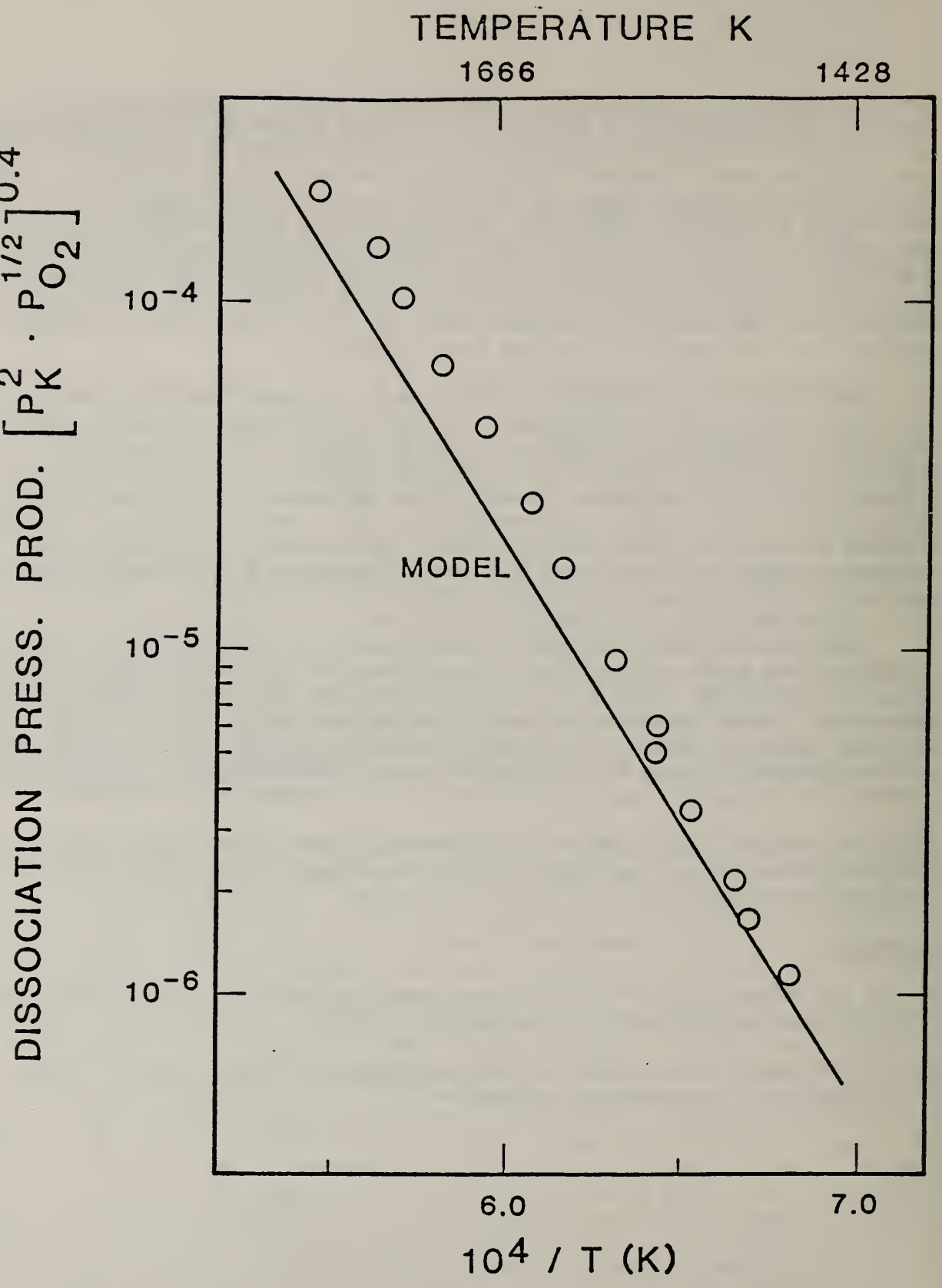

Figure 1. Comparison of $(P_K^2 \cdot P_{O_2}^{1/2})^{0.4}$ vs $10^4/T$ with line predicted by model equation. $(P_K^2 \cdot P_{O_2}^{1/2})^{0.4}$ is equivalent to P_K for system in which $P_{O_2} = P_K/4$. Slag composition is 47.3 wt.% SiO_2, 11.1 Al_2O_3, 12.0 Fe_2O_3, 13.9 CaO, 7.0 MgO, and 8.7 K_2O. Modified slag composition for model line is 47.3 wt.% SiO_2, 23.1 Al_2O_3, 20.9 CaO, and 8.7 K_2O.

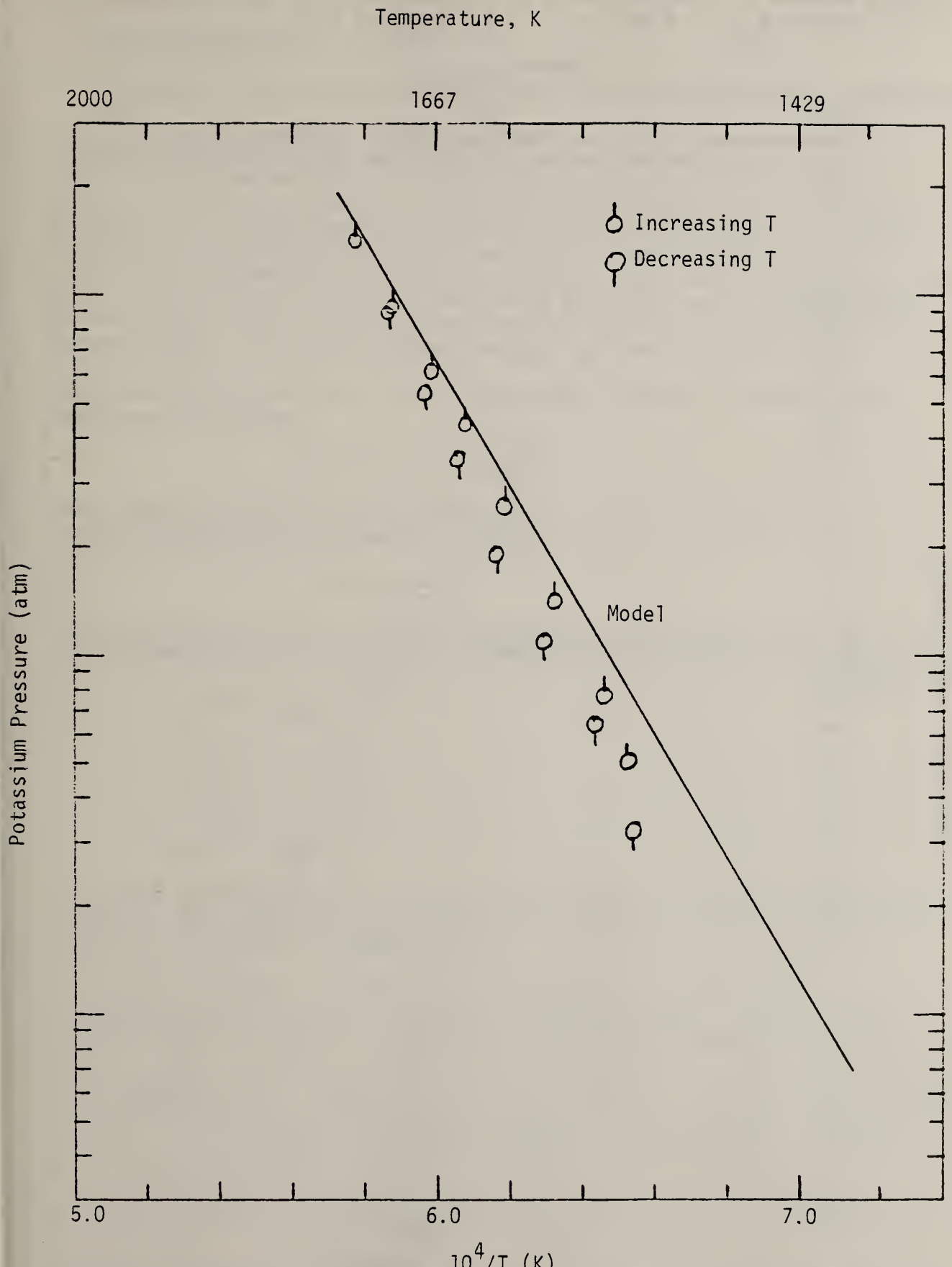

Figure 2. Comparison P_K over Western channel slag having a K_2O concentration varying between 18.9 and 17.6 wt.% K_2O compared with the model prediction with 18.2 wt.% K_2O, 13.3 CaO, 31.8 Al_2O_3, and 36.7 SiO_2.

Figure 3. Comparison P_K over Western channel slag having a K_2O concentration varying between 12.9 and 10.8 wt.% K_2O compared with the model prediction with with 11.8 wt.% K_2O, 14.4 CaO, 34.2 Al_2O_3, and 39.6 SiO_2.

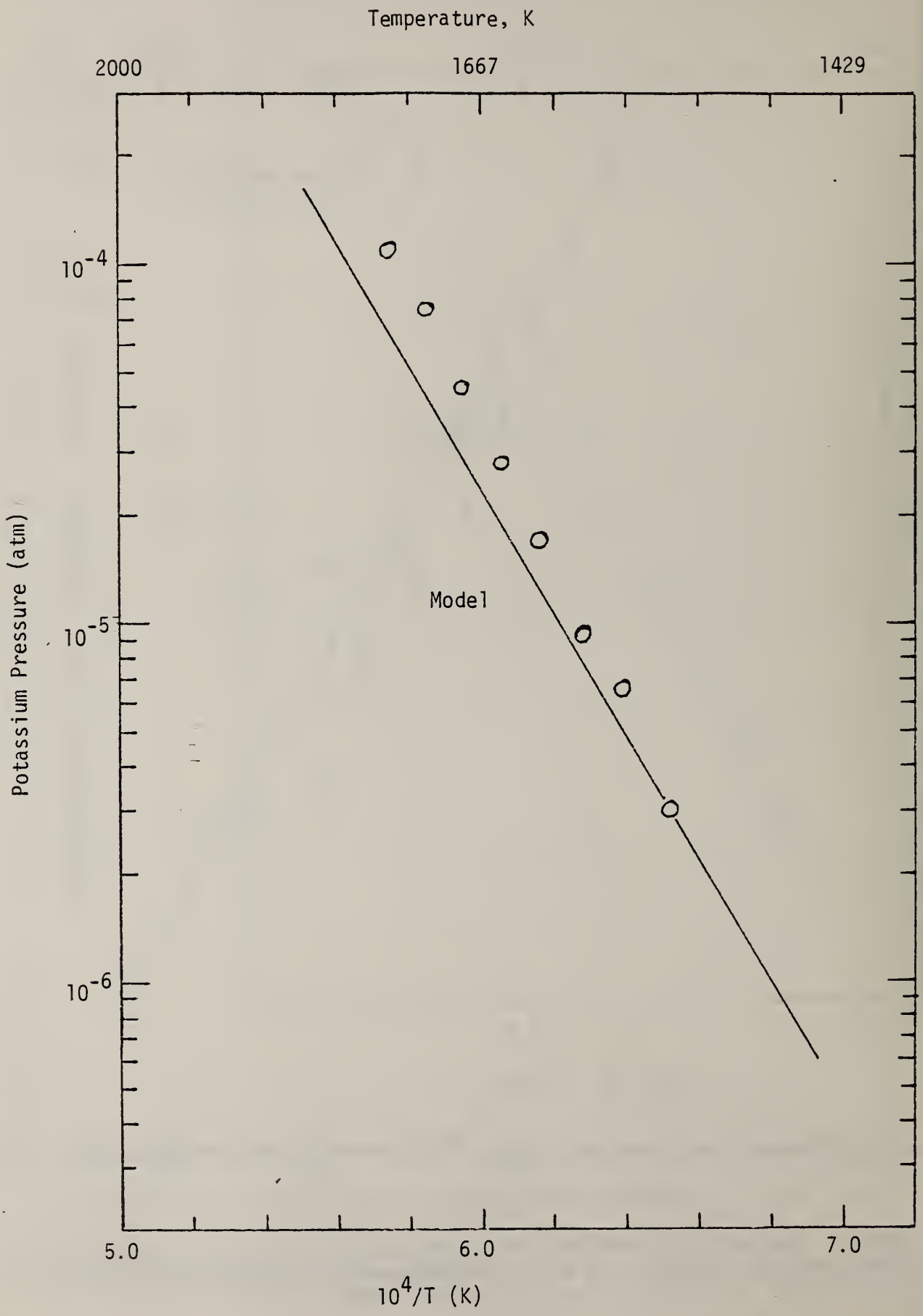

B. Phase Equilibria (L. P. Cook)

1. Phase Equilibrium-derived Model for the Calculation of Activity Coefficients

As noted in previous quarterly reports [1], knowledge of subsolidus equilibria can be used to derive an independent estimate of potassia activities in the melt phase in the system K_2O-CaO-Al_2O_3-SiO_2. This is done by fitting a function to the activities calculated from thermodynamic properties of solids involved in invariant melting reactions. By combining topological constraints with the Gibbs-Duhem solutions for the system, it is, in principle, possible to derive a model which is capable of predicting K_2O activities to within an order of magnitude or better over a large compositional range. The principal assumptions are heat capacity expressions for the melt phase, and in some cases, Henry's Law coefficients.

The Gibbs-Duhem equations can be summarized as a series of differential equations of the form

$$-SdT + VdP - \Sigma X_i d\mu_i = 0.$$

These equations apply of course only at equilibrium, and specifying constant temperature and pressure leads to:

$$\Sigma X_i d\mu_i = 0.$$

These equations include a non-ideal term usually expressed by way of an activity coefficient, γ_i. Thus the differential equations of interest are:

$$X_{CaO} d\ln \gamma_{CaO} = 0$$

$$X_{Al_2O_3} d\ln \gamma_{Al_2O_3} = 0$$

$$X_{SiO_2} d\ln \gamma_{SiO_2} = 0$$

$$X_{K_2O} d\ln \gamma_{K_2O} = 0$$

A solution to equations of this type is customarily presented in power series form [2]. For quaternary K_2O-CaO-Al_2O_3-SiO_2 melts, an expression for the activity coefficient of potassia is:

$$\ln\gamma_{K_2O} = \sum_{j=1}^{4} \left((2\ln\gamma^{D}_{j\text{-}K_2O} - \ln\gamma^{D}_{K_2O\text{-}j}) X_j^2 + 2(\ln\gamma^{D}_{K_2O\text{-}j} - \ln\gamma^{D}_{j\text{-}K_2O}) X_j^3 \right) +$$

$$\sum_{j=1}^{4}\sum_{k=1}^{4} \left(1/2(3\ln\gamma^{D}_{k\text{-}K_2O} + 3\ln\gamma^{D}_{j\text{-}K_2O} - \ln\gamma^{D}_{K_2O\text{-}j} - \ln\gamma^{D}_{K_2O\text{-}k} - \ln\gamma^{D}_{j\text{-}k} - \ln\gamma^{D}_{k\text{-}j}) X_j X_k + \right.$$

$$\left. (3\ln\gamma^{D}_{K_2O\text{-}j} - 3\ln\gamma^{D}_{j\text{-}K_2O} + \ln\gamma^{D}_{K_2O\text{-}k} - \ln\gamma^{D}_{k\text{-}K_2O} + \ln\gamma^{D}_{j\text{-}k} - \ln\gamma^{D}_{k\text{-}j}) X_j^2 X_k \right) +$$

$$\sum_{j=1}^{4}\sum_{k=1}^{4}\sum_{m=1}^{4} (\ln\gamma^{D}_{j\text{-}K_2O} + \ln\gamma^{D}_{k\text{-}K_2O} + \ln\gamma^{D}_{m\text{-}K_2O} - \ln\gamma^{D}_{K_2O\text{-}j} - \ln\gamma^{D}_{K_2O\text{-}k} - \ln\gamma^{D}_{K_2O\text{-}m}) X_i X_k X_m$$

where 1 = K_2O, 2 = CaO, 3 = Al_2O_3, 4 = SiO_2, and γ_i^D is the activity coefficient at infinite dilution.

As can be seen, according to this formulation only 12 constants, γ_{i-j}^D are required. These are:

1. $\gamma_{K_2O-CaO}^D$
2. $\gamma_{CaO-K_2O}^D$
3. $\gamma_{K_2O-Al_2O_3}^D$
4. $\gamma_{Al_2O_3-K_2O}^D$
5. $\gamma_{K_2O-SiO_2}^D$
6. $\gamma_{SiO_2-K_2O}^D$
7. $\gamma_{CaO-Al_2O_3}^D$
8. $\gamma_{Al_2O_3-CaO}^D$
9. $\gamma_{CaO-SiO_2}^D$
10. $\gamma_{SiO_2-CaO}^D$
11. $\gamma_{Al_2O_3-SiO_2}^D$
12. $\gamma_{SiO_2-Al_2O_3}^D$

Of these, reasonable estimates of coefficients #5, 7, 8, 9, 10, 11 and 12 can be made [3]. In the forthcoming quarter a least squares fit, probably using a Henry's Law approximation with linear temperature dependence, will be made to the remaining coefficients. If the fit is reasonable, further refinements will be made and the model will be tested as far as possible.

2. Calculations of Liquidus Surfaces in the System K_2O-CaO-Al_2O_3-SiO_2

One of the goals of the phase equilibrium portion of the slag thermochemistry project is the build-up of a body of experimental data describing the melting behavior of carefully selected slags. Another goal is the development, from this data base, of models capable of accurately predicting the crystallization and melting behavior of complex multicomponent slags over a broad range of composition and temperature. Detailed knowledge of melting/crystallization behavior as a function of composition is essential for understanding and accurately predicting the behavior of slag in the combustor, channel, and diffuser, where components are designed to operate under a specific range of slag flow properties. The ratio of crystals to melt in any given slag affects not only viscosity but also electrical conductivity, corrosiveness and the ability to wet ceramic or metal surfaces.

Silicate slags of the type found in MHD systems are among the most complex of solutions - a typical MHD slag contains more than seven oxide components. It is generally accepted that slags can be regarded as ionic solutions, and it is thought that they are composed of simple cations such as K^{+}, Ca^{+2}, Na^{+}, Mg^{+2}, Fe^{+2}, etc. and a considerable range of anions, primarily polymers of the type $[Si_N O_{2N+y}]^{-2y}$. In spite of such complexity, it has been recognized in recent years that application of polymer solution theory yields, in certain cases, a reasonably good fit to the experimental data which is encouraging, because this model is developed primarily from a well-defined structural theory, rather than from an empirically derived function. Accurate prediction of phase equilibrium properties over a range of compositions requires just such a structural model to provide the understanding of the actual species distribution needed for thermodynamic calculation. This is true because in the absence of a unifying structural theory, one must employ strictly a empirical approach involving the use of fitted excess functions and the results cannot be expected to be reliable in the general case, for complex slags without the availability of an enormous amount of data, generally not available. Unlike the prediction of some properties such as viscosity, where for some purposes precision of an order of magnitude will suffice, prediction of melting properties requires precision of at least a few tens of degrees and at least ∿10 mole %. For these reasons the polymer ionic solution model has been developed for MHD slags as outlined below, in the hope that ultimately this model may become reliable enough to provide estimates to be used in system operation.

The essential features of the quasichemical model of melt polymerization (QCP) have been outlined in previous quarterly reports [4], and as noted, one of the prime difficulties in applying this model is the treatment of aluminum. During the past quarter an attempt was made to find a reasonable treatment of Al_2O_3 in terms of the model, by considering phase equilibria in the system K_2O-CaO-Al_2O_3-SiO_2. Six binary systems on the "faces" of the quaternary were used an input: anorthite-silica, anorthite-wollastonite, anorthite-corundum, $KAlSiO_4$-corundum, leucite-corundum, and wollastonite-silica. As a test of the model, an attempt was then made to fit data for the system anorthite-leucite, a join lying "inside" the quaternary tetrahedron.

There are essentially two alternatives for the treatment of aluminum. One involves coupled solution of calcium and aluminum in the melt, the other considers aluminum to be present in the melt as an independent species. Although data for the system anorthite-silica can be modeled reasonably well using a calcium aluminate species, this does not appear to provide a reasonable fit for the other systems. Attention has thus been focused on the second alternative for solution of alumina. Possibilities include both positively and negatively charged species. In keeping with the amphoteric nature of alumina it has been assumed that in compositions with atomic K:Al <1, some of the alumina will be present as positively charged species. Thus it is necessary to define an equilibrium constant for the quasichemical reaction:

$$Al_{.67}O \rightarrow .67(Al^{+3}) + O^{-2}$$

Figure 1 shows the effect of different values of the dissociation equilibrium constant for aluminum on the melt chemistry for the eutectic composition in

the system anorthite-wollastonite. A change from K = 4 to K = 4000 increases the proportion of non-bridging oxygens in the melt substantially. A value of K ≃ 40 at 1500 °C appears to fit the liquidus data for the six binary systems best. This is a reasonable value for a strongly associated oxide [5].

The following precipitation reactions have been used. These reactions are also quasichemical in that they do not involve charge balance [6]. Charge balance is important in determining the mixing behavior of the melt, but at the precipitation sites, electrical neutrality must be maintained, presumably by free diffusion of O^{-2} ions toward or away from the reaction site. Hence, the activity of the precipitating phase is defined only in relation to the primary species taking part.

$$(Al_{.67}O)_{corundum} \rightleftarrows 1/M\ (Al_{.67M}O_M)$$

$$(SiO_2)_{cristobalite} \rightleftarrows 1/N\ (Si_NO_{2N})$$

$$(CaAl_2Si_2O_8)_{anorthite} \rightleftarrows CaO + 3/M\ (Al_{.67M}O_M) + 2/N\ (Si_NO_{2N})$$

$$(CaSiO_3)_{wollastonite} \rightleftarrows CaO + 1/N\ (Si_NO_{2N})$$

$$(KAlSiO_4)_{crystal} \rightleftarrows 1/P\ (K_PAl_PO_{2P}) + 1/N\ (Si_NO_{2N})$$

$$(KAlSi_2O_6)_{leucite} \rightleftarrows 1/P\ (K_PAl_PO_{2P}) + 2/N\ (Si_NO_{2N})$$

If an "ideal activity" is defined according to:

$$a = e^{-\left(\frac{\Delta H^{fusion}}{R}\left(\frac{1}{T} - \frac{1}{T_{fusion}}\right)\right)}$$

these activities as a function of temperature can be compared - on the assumption that the QCP model correctly accounts for solution nonideality - with those calculated according to the following equations which apply at saturation:

$$a_{corundum} = \gamma^o_{corundum}\ (X_{Al_{.67M}O_M})^{1/M}$$

$$a_{cristobalite} = \gamma^o_{cristobalite}\ (X_{Si_NO_{2N}})^{1/N}$$

$$a_{anorthite} = \gamma^o_{anorthite}\ (X_{CaO})(X_{Al_{.67M}O_M})^{3/M}\ (X_{Si_NO_{2N}})^{2/N}$$

$$a_{wollastonite} = \gamma^o_{wollastonite}\ (X_{CaO})\ (X_{Si_NO_{2N}})^{2/N}$$

$$a_{KAlSiO_4} = \gamma^o_{KAlSiO_4}(X_{K_PAl_PO_{2P}})^{1/P}\ (X_{Si_NO_{2N}})^{1/N}$$

$$a_{KAlSi_2O_6} = \gamma^o_{KAlSi_2O_6}(X_{K_PAl_PO_{2P}})^{1/P}\ (X_{Si_NO_{2N}})^{2/N}$$

where γ^o is a constant defined by the requirement that the activity of the crystal in its own melt is unity. Note that the model allows considerable lattitude in varying the multiplicity of the "clusters"* taking part in the precipitation reactions, indicated by the variables M, N, P.

Algorithms have been devised to determine the values of M, N, and P for each of the six binary systems input which optimize the simultaneous fit for both liquidus curves in each binary at the eutectic point. These algorithms also perform calculations of structon probabilities in each melt composition so that the precipitation reaction can be accurately described in terms of the anionic polymeric species involved. The rule which has been employed in defining precipitation reactions in terms of structon proportions is that no Si-O bonds be broken during the precipitation process. This is consistent with the simple notion that precipitation is essentially a bond-building process while solution is essentially a bond-breaking process. This in the case of wollastonite precipitation, all structons with less than 3 bridging oxygens are involved, whereas in the case of cristobalite, all structons participate.

Results of fitting the QCP model to the six binary eutectics are illustrated in figures 2-7 for various clustering parameters. The conclusion is that values of M $\simeq$ 4.5, N $\simeq$ 3 and P>4 fit the data best. The fit for the silica liquidus seems to require very large values of N, however. This is inconsistent with the values required for anorthite and wollastonite in the same melts. This discrepancy is not surprising in view of the miscibility gap near the silica end in many binary systems, in particular the system wollastonite-silica, and it is obvious that for very silica-rich melts the QCP model must be modified. Apart from the silica liquidii, most of the surfaces in the six binary systems are represented to within 50 °C and 10 mol % by the QCP model.

The values of the parameters, M, N, P should be discussed. For aluminum species, M = 4.5 corresponds to three Al atoms. It has been assumed that this species is positively charged. The tetrahedral cluster $[Al_3O_4]^{+1}$ is one possibility. If M = 6 is allowable, then trigonal dipyramid $[Al_4O_5]^{+2}$ is a possibility. Turning to silica, values of N = 3 might correspond to $[Si_3O_{10}]^{-8}$. Again, if slight variation is allowed to N = 4 then $[Si_4O_{12}]^{-8}$ is a possibility. Note that a substantial range in structon proportions is represented by combining these species with higher polymers such as $[Si_NO_{2N+4}]^{-8}$.

While figures 2-7 show that the QCP model gives a reasonable first-order fit to the six binary systems with relatively few assumptions, the validity of these assumptions must be verified more rigorously. However, a preliminary test of the model can be made on the system anorthite-leucite, a binary join <u>within</u> the system K_2O-CaO-Al_2O_3-SiO_2. Results are shown in figure 8. Cluster parameters were chosen on the basis of the six previous binary fits as M = 4.5, N = 3, P = 4. The fit to the anorthite liquidus is

*Here used as a general term applied to charged or neutral species containing more than one metal atom.

somewhat disappointing, although quite good for the leucite liquidus. However, it may be significant the anorthite fit improves markedly if $P \cong 8$ is employed (not shown), corresponding perhaps to the cubic species $[K_8Al_8O_{12}]^{-8}$. (Note the similarity in charge of this species to that of the silicate anions suggested above, raising the conjecture that perhaps equality of charge is of prime importance in mixing on the anionic sublattice).

Before the QCP model can be tested further, it will be necessary to refine it somewhat to allow cluster parameters to vary as a function of melt composition. In the present model, M, N and P are identical in melt and standard state. The ultimate aim is of course to produce a theoretically self-consistent model capable of giving liquidus surfaces to within 50 °C and 10 mole % over the entire range of K_2O-CaO-Al_2O_3-SiO_2 aluminosilicate rich melts without new input. A concerted theoretical effort aided by experimental results could produce highly valuable results. However, it is doubtful that this can be accomplished during the present fiscal year.

Plans

1. Attempt least squares fit to constants of phase equilibrium-derived quaternary potassia activity model.

2. Develop theoretical basis for QCP model in order to improve accuracy of liquidus predictions.

3. Gather and input additional experimental data to test QCP model.

References

1. S. J. Schneider, MHD Materials - Seed/Slag Interactions and Effects, NBS Quarterly Progress Report, October 1 - December 31, 1980, p. 5.

2. K. L. Currie and L. W. Curtis, J. Geol. 84, 179 (1976).

3. a. E. R. Plante, NBS Spec. Publ. 561, p. 265-281 (1979).
   b. D. A. R. Kay and J. Taylor, Trans. Far. Soc. 56, 1372 (1960).
   c. J. C. Fulton and J. Chipman, Trans. AIME J. Metals 6, 1136 (1954).
   d. F. C. Langenberg, H. Kaplan and J. Chipman, Conf. Phys. Chem. Steelmaking, American Iron & Steel Inst., p. 65-67 (1956).

4. S. J. Schneider, MHD Materials - Seed/Slag Interactions and Effects, NBS Quarterly Progress Report, January - March 1980.

5. C. K. Mason, J. Amer. Ceram. Soc. 51, 134 (1968).

6. D. G. Fraser, Thermodynamic Properties of Silicate Melts, p. 301 in D. G. Fraser, ed., Thermodynamics in Geology, Proc. Natl. Adv. Study Inst., Reidel (1977).

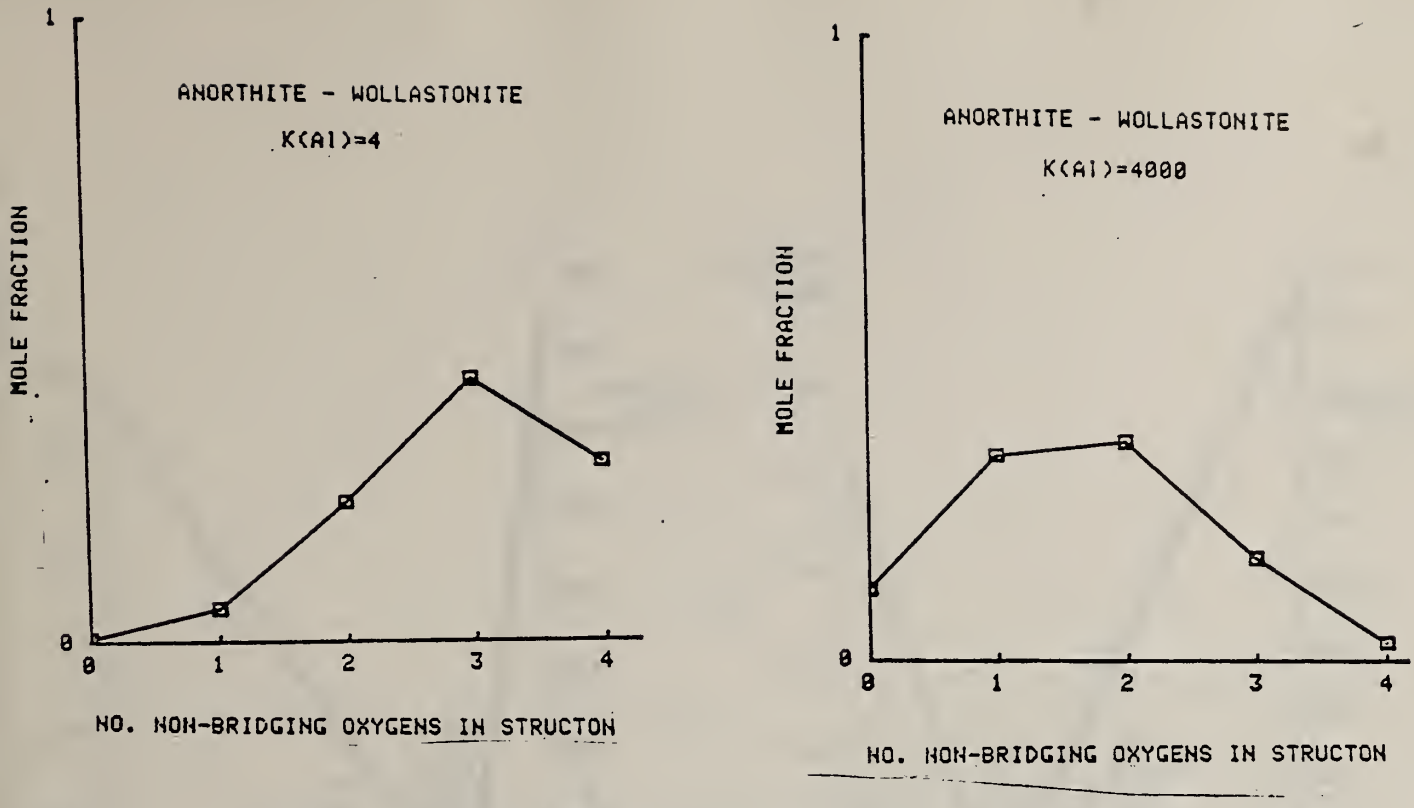

Figure 1. Variation of structon proportions in anorthite-wollastonite eutectic for two different values of the Al dissociation constant. K = 4 (left diagram), vs. K = 4000 (right diagram). Note dramatic change in number of non-bridging oxygens.

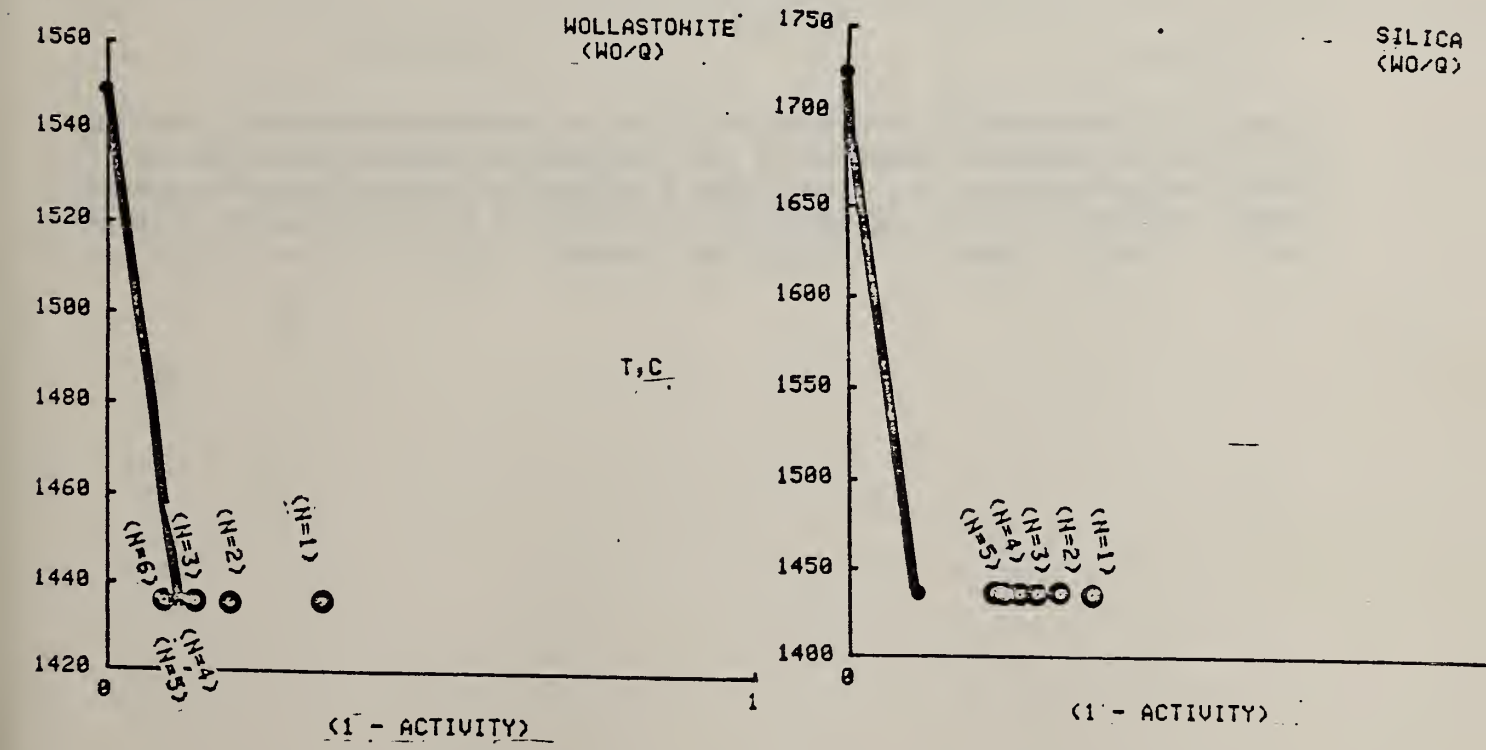

Figure 2. Comparison of ideal activity in system wollastonite-silica with QCP activities at eutectic temperature for different silica polymerizations (N). Wollastonite liquidus on left, silica liquidus on right. QCP activity at end member mp's is unity. Eutetic data are from Bowen, Schairer and Poznak, Amer. J. Sci. 26, 195 (1933).

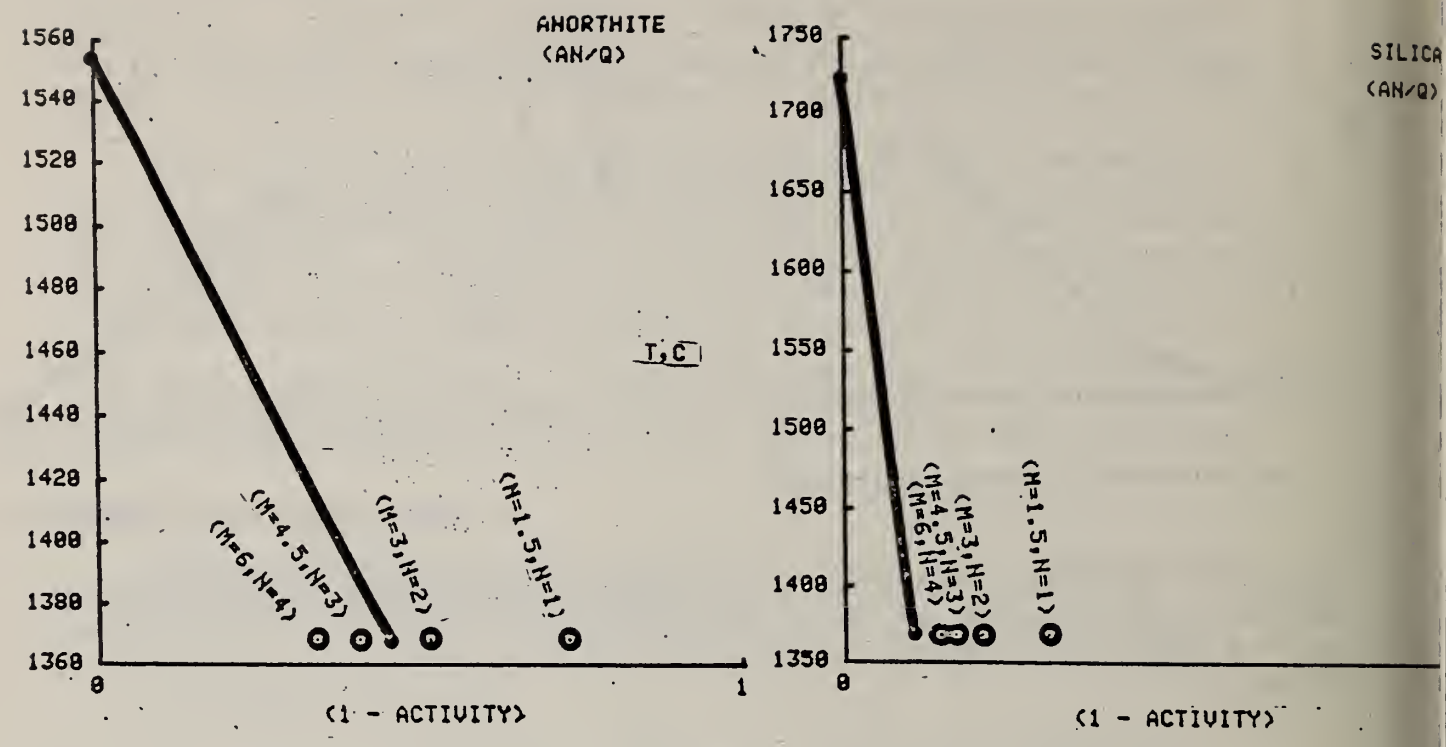

Figure 3. Comparison of ideal activity in system anorthite-silica with QCP activities at eutectic temperature for different aluminum species (M) and silica polymerizations (N). Anorthite liquidus on left, silica liquidus on right. QCP activity at end member mp's is unity. Data are from G. A. Rankin and F. E. Wright, Amer. J. Sci. 39, 45 (1915).

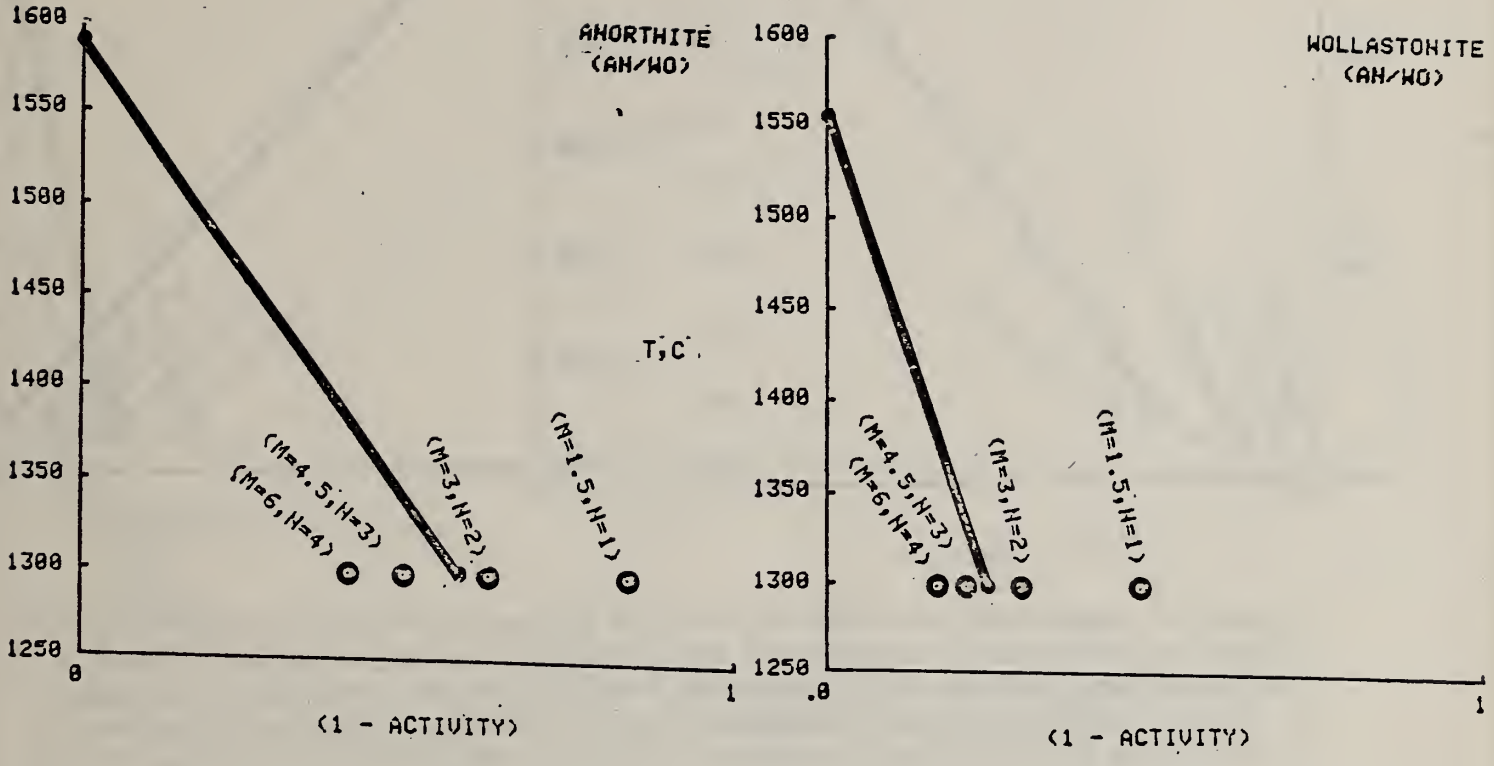

Figure 4. Comparison of ideal activity in system anorthite-wollastonite with QCP activities at eutectic temperature for different aluminum species (M) and silica polymerizations (N). Anorthite liquidus on left, wollastonite liquidus on right. QCP activity at end member mp's is unity. Eutectic data are from G. A. Rankin and F. E. Wright, Amer. J. Sci. 39, 45 (1915).

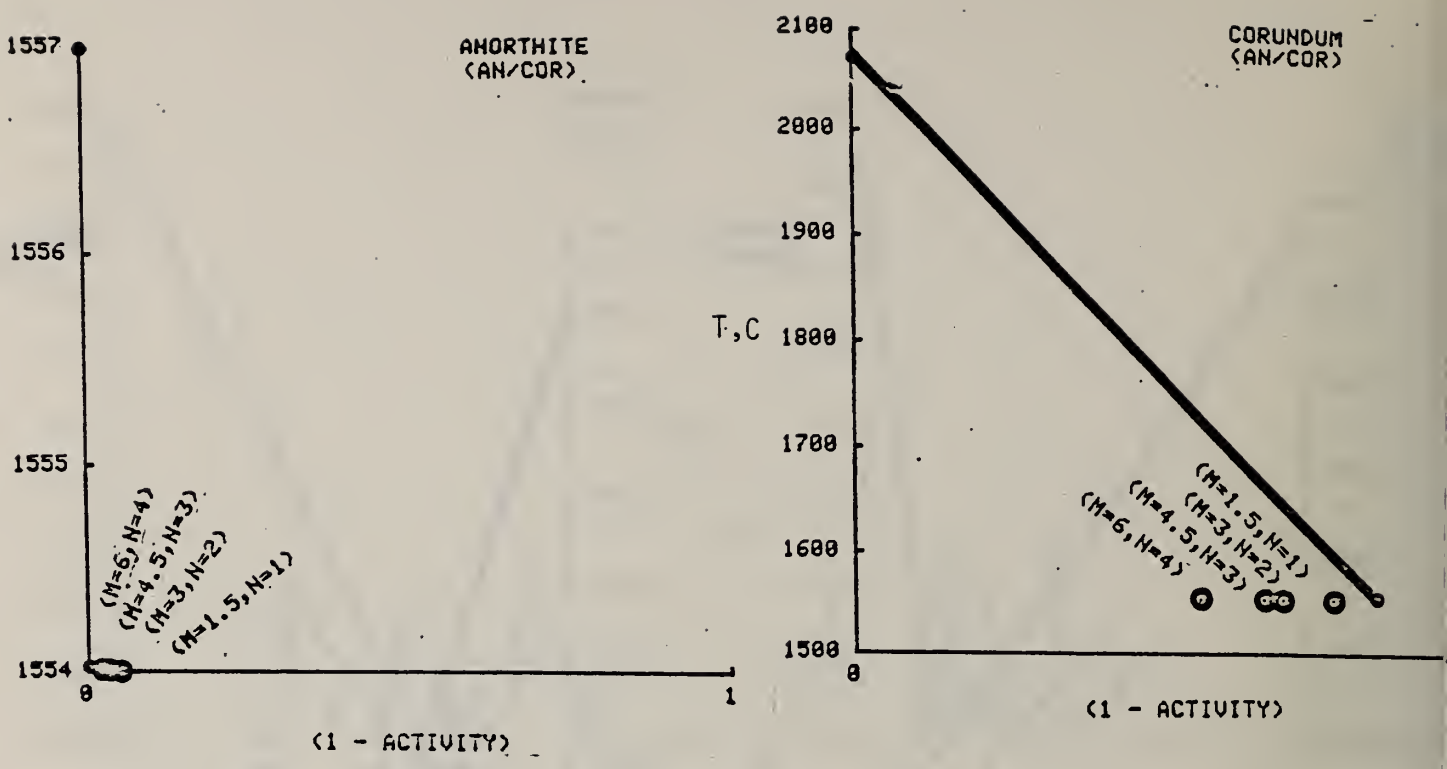

Figure 5. Comparison of ideal activity in system anorthite-corundum with QCP activities at eutectic temperature for different aluminum species (M) and silica polymerizations (N). Anorthite liquidus on left, corundum liquidus on right. QCP activity at end members mp's is unity. Eutectic data from G. A. Rankin and F. E. Wright, Amer. J. Sci. 39, 46 (1915).

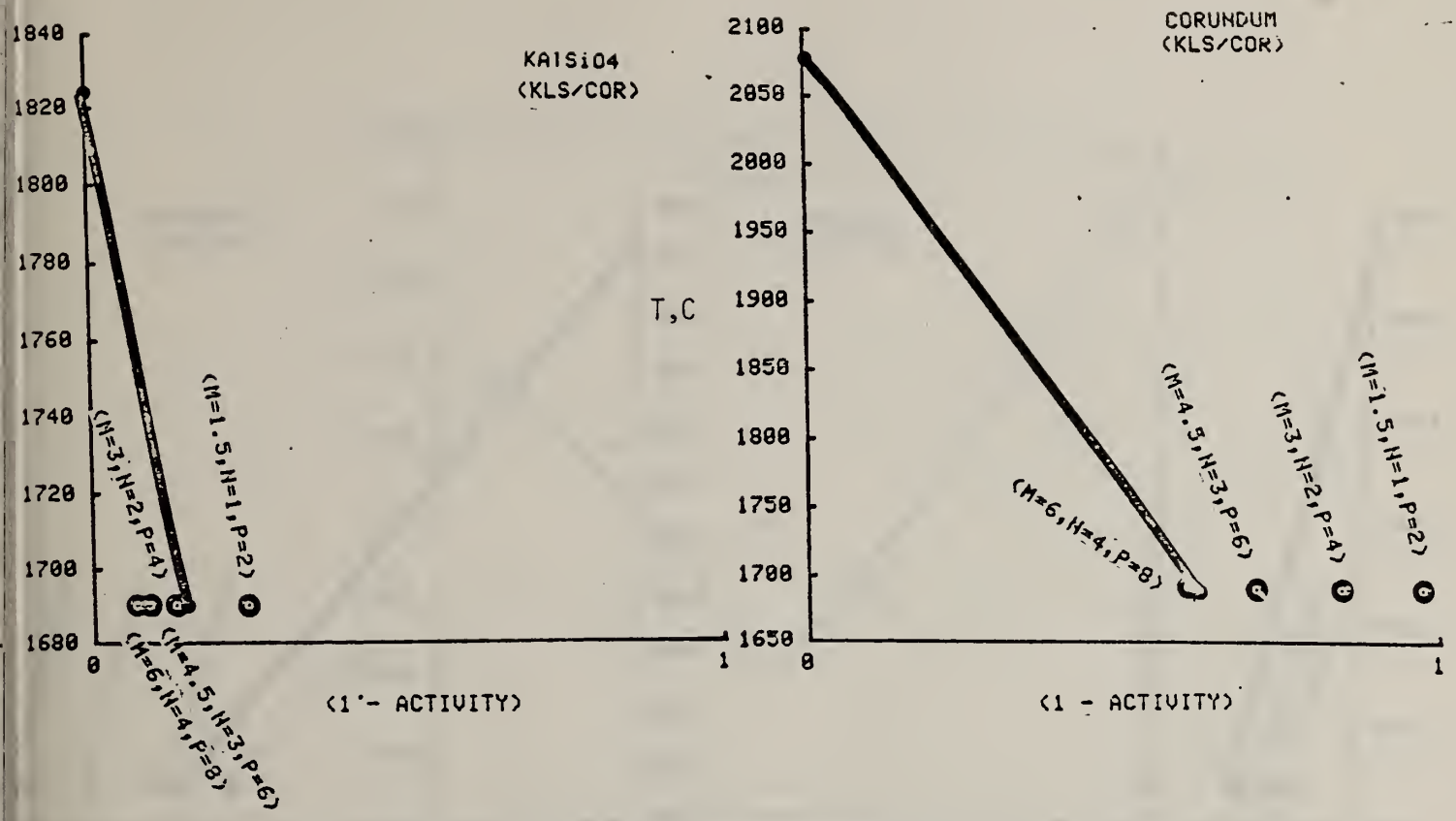

Figure 6. Comparison of ideal activity in system $KAlSiO_4$-corundum with QCP activities at eutectic temperature for different aluminum species (M) and silica polymerizations (N) and potassium aluminate species (P). QCP activity at end member mp's is unity. Eutectic data are from J. F. Schairer and N. L. Bowen, Amer. J. Sci. 253, 719 (1955).

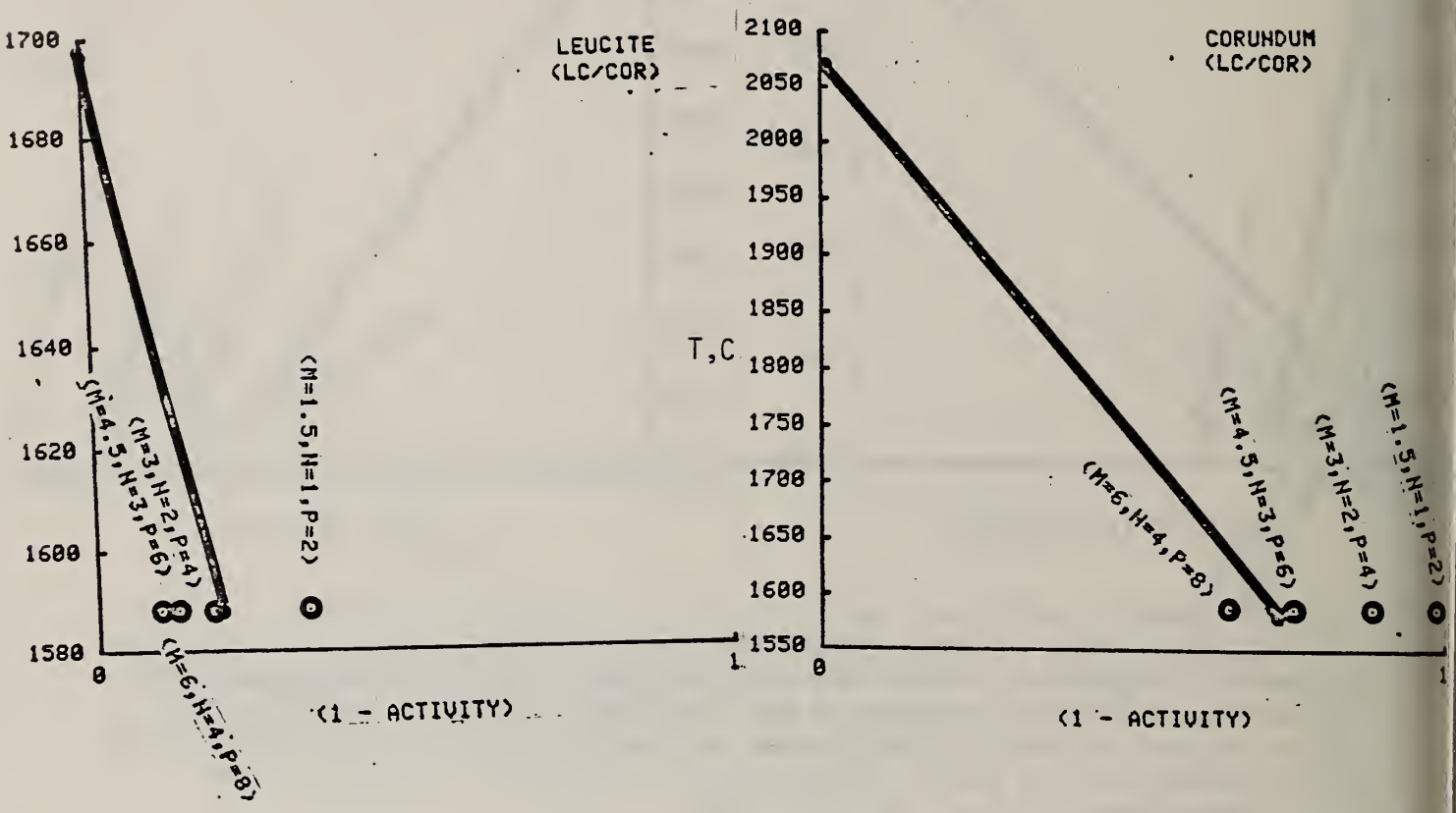

Figure 7. Comparison of ideal activity in system leucite-corundum with QCP activities at eutectic temperature for different aluminum species (M), silica polymerizations (N) and potassium aluminate species (P). QCP activity at end member mp's is unity. Eutectic data are from J. F. Schairer and N. L. Bowen, Amer. J. Sci., 253 718 (1955).

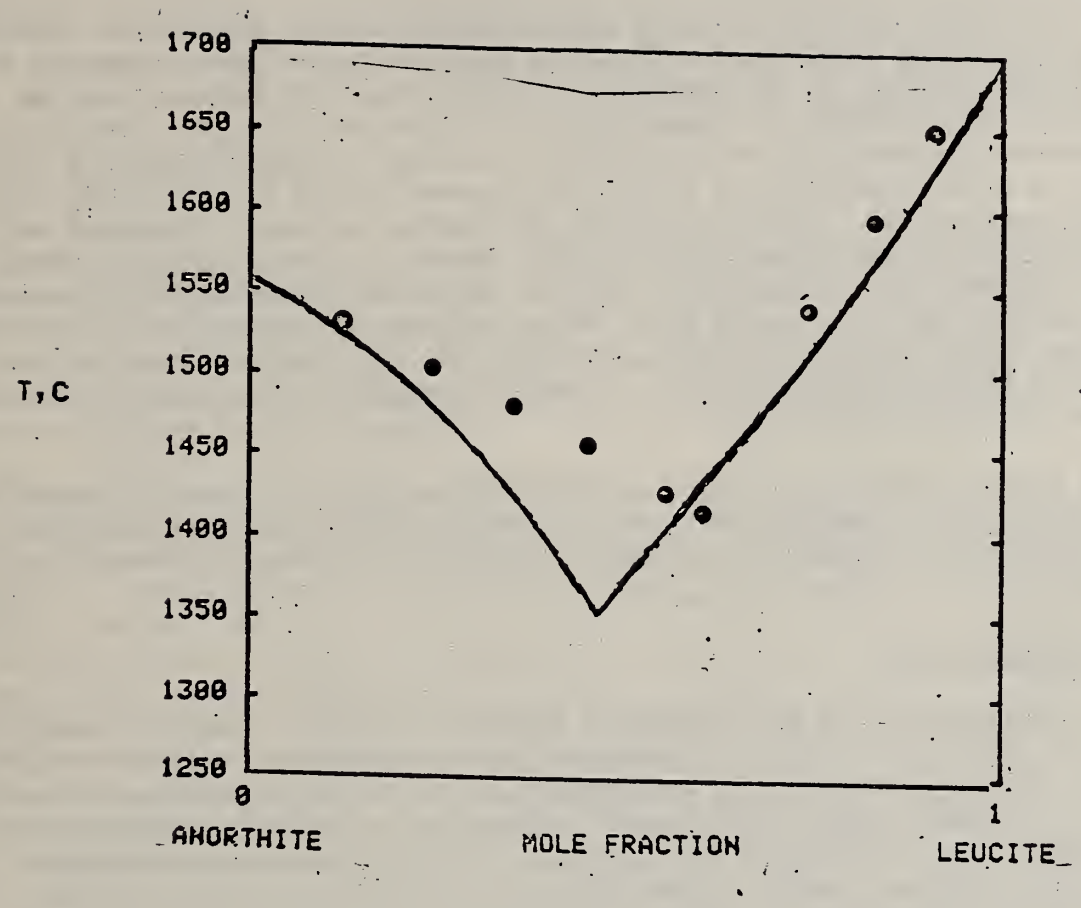

Figure 8. Comparison of experimental data for system anorthite-leucite with *a priori* QCP calculation (solid curves) assuming M = 4.5, N = 3, P = 6. Data are from J. F. Schairer and N. L. Bowen, Amer. J. Sci. 245, 193 (1947).

2. Electrical Conductivity and Polarization (W. R. Hosler)

Progress

Introduction

In the last quarterly report (January-March 1981) electrical conductivity data on a typical Western slag (Rosebud seam, Montana) were presented with an analysis related to the specific impedance measured between all the probe sets for a number of temperatures. To properly present the DC data, an averaging method must be used when conducting ion mobilities are high enough to cause polarization at the electrodes during the 40 second period of data acquisition for each polarity of applied voltage. This had not been done previously and is presented in this report. Quenching experiments were also described in the last report. These are necessary to correlate the conductivity of a sample after being held at a temperature for a long time and having reached a stable condition to the physical state of the sample in that stable condition. Some SEM and XRD work on these quenched samples has been completed.

A paper, Electrical Conductivity of Mixed Ionic/Electronic Conducting Materials at High Temperatures, was presented at the International Joint Conference on Thermophysical Properties, National Bureau of Standards, Gaithersburg, MD, June 15-18, 1981.

Slag Conductivity

As pointed out in most previous quarterly reports, the absolute value of a measured conductivity is dependent on the previous treatment of a slag sample. For that reason,it is necessary to set a definite procedure of sample treatment before measurement in order to be able to characterize the sample condition during measurement. In this case, measurements were taken with decreasing temperature after soaking at a particular temperature long enough to reach a stabilized conductivity. This stabilization period allows the slag body to reach a nearly equilibrated oxidation/reduction condition, as well as a crystalline/glassy composition for that temperature and slag composition. The format for taking data was given in the previous two quarterly reports, along with the definitions of $F_{12}(V)$ and $F_{34}(V)$. In the DC case, an averaging process should be used to determine polarization effects when conducting ion mobilities are large enough to allow polarization to take place during the 40 seconds required for acquiring the data for each applied voltage direction. It is necessary to reverse the current at each temperature point to account for any thermoelectric voltage that might be present due to a temperature gradient along the sample, but, more importantly, to minimize any permanent polarization due to an ion concentration build up at a given electrode. For this case, an average anode and cathode F(V) function may be defined as

$$\text{average anode } F(V) = \frac{F^{+}_{12}(V) + F^{-}_{34}(V)}{2}$$

$$\text{average cathode } F(V) = \frac{F^{-}_{12}(V) + F^{+}_{34}(V)}{2}$$

Figure 1 shows a plot of these anode and cathode F(V) values as a function of temperature. At high temperature, where the viscosity is low (and ion mobility high), there is a large difference between the anode and cathode values, possibly due to polarization at the cathode where positive ions should migrate. At low temperatures, where the slag is highly viscous or solid, the difference between the anode and cathode values is small. It has not been established, in this material, that the conducting ion is iron, as was the case for the Bow, NH (Eastern) slag reported previously.

SEM, EDX and XRD Analysis

The last sample on which the conductivity was measured was sectioned for analysis. This sample had been heated to near 1500 °C and then cooled slowly while collecting stabilized conductivity points to 700 °C and subsequently cooled to room temperature. It was sectioned into four pieces, each containing a probe. All sections showed essentially the same topography with no differences being observed near a current carrying electrode (1 and 4) or near a voltage probe (2 and 3).

Figure 2 shows a micrograph of a region of the sample containing the lower current carrying probe (probe 4) at 20X. At this magnification and in figure 3, which is area A of figure 2 at 100X, it can be seen that the platinum is rather porous. Figure 4 is a micrograph of area B in Figure 3 at 512X. The very light area is platinum. Figure 5 is area C in Figure 4 at a magnification of 2000X and shows the platinum slag interface in detail. Figures 6a and 6b are EDAX spectra of the areas designated 1, 2, 3 and 4 of figure 5. Area 1 is platinum with no diffused iron detected. This was of some concern during the course of the measurements since platinum is known to permit iron diffusion in some cases where it is used to contain high iron content materials. Apparently it does not happen in this case even though the electrodes are relatively porous. Scan 2 of figure 6a shows the content of a medium grey area. It contains essentially aluminum, silicon and potassium and is most likely the potash feldspar ($KAlSi_3O_8$) or leucite ($KAlSi_2O_4$) as determined by XRD and reported in the last quarterly report. Scan 3 of figure 6b shows the content of a lighter grey area near the electrode. It contains iron and aluminum with a small amount of magnesium and could be the iron-alumina spinel detected by XRD. Finally, scan 4 of figure 6b is essentially the same as scan 2 and represents the same material as described previously. This material makes up the main part of the slag and is not a conducting material in its crystalline state. The iron-alumina spinel found in the area of scan 3 is a conducting material, the conductivity depending on the oxidation/reduction state of the iron in the crystalline material. This material is considerably less in amount than the leucite or potash feldspar as can be seen from figure 4 where the light grey areas are spinel in an extensive background of leucite or potash feldspar. Bridging of the conducting material does not appear evident here and the conductivity path through the material is not known.

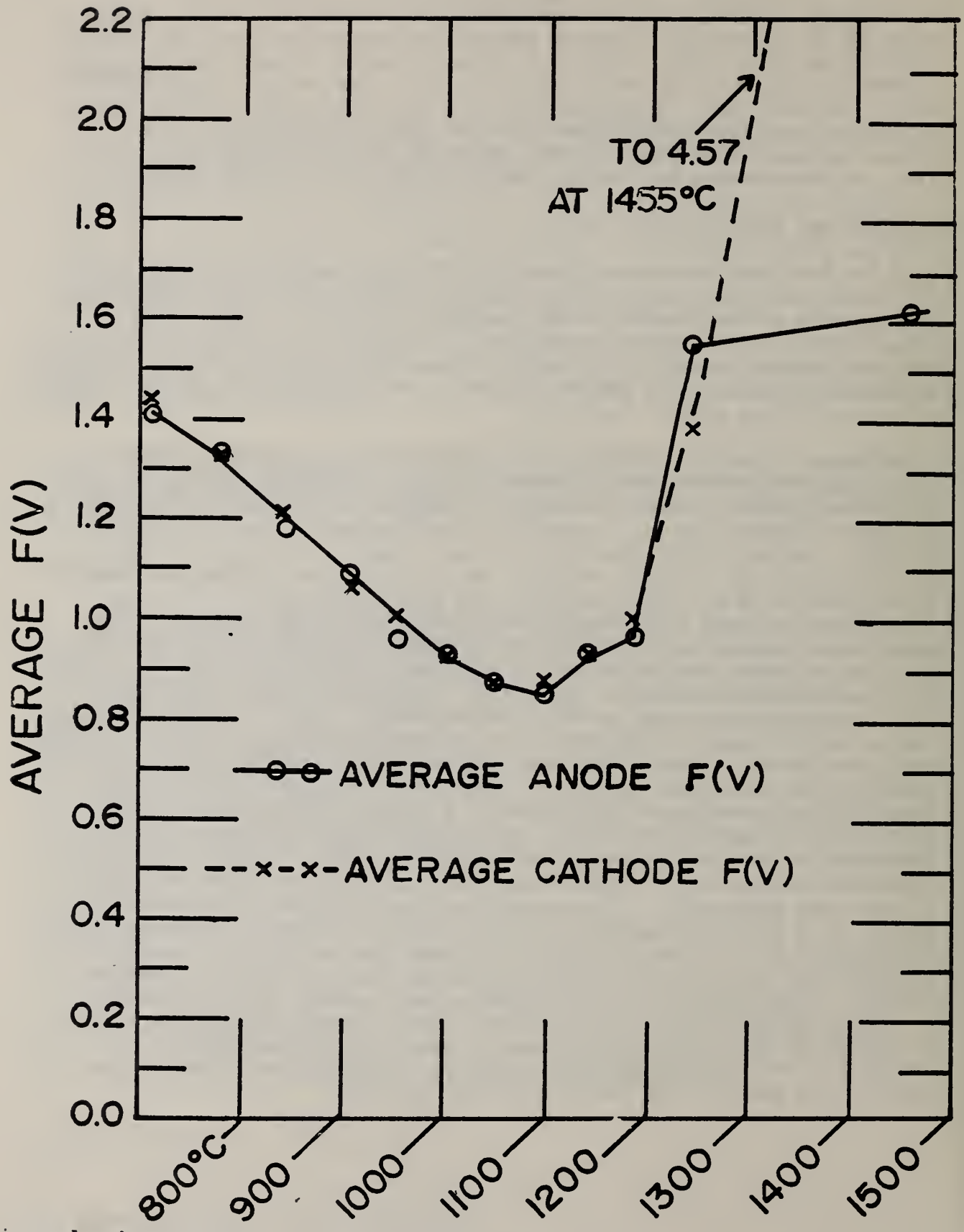

Figure 1. Average anode and cathode functions (see text) vs. temperature up to near 1500 °C.

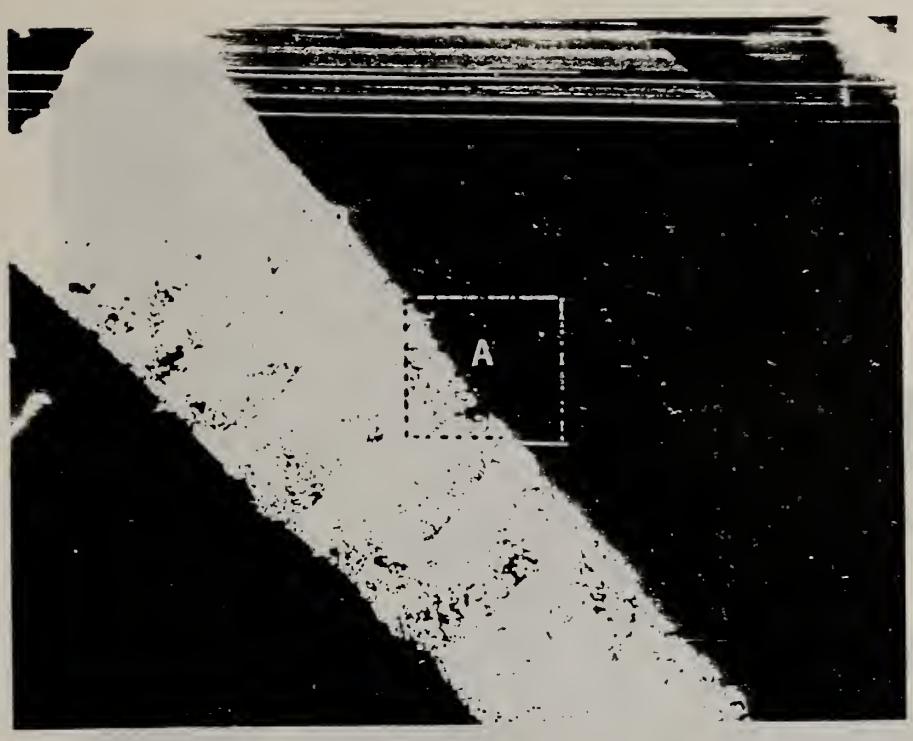

Figure 2. SEM micrograph of a region of sample containing a lower current carrying probe (light material running from upper left to lower right). The slag in this series of micrographs is derived from coal from the Rosebud seam in Montana. 20X.

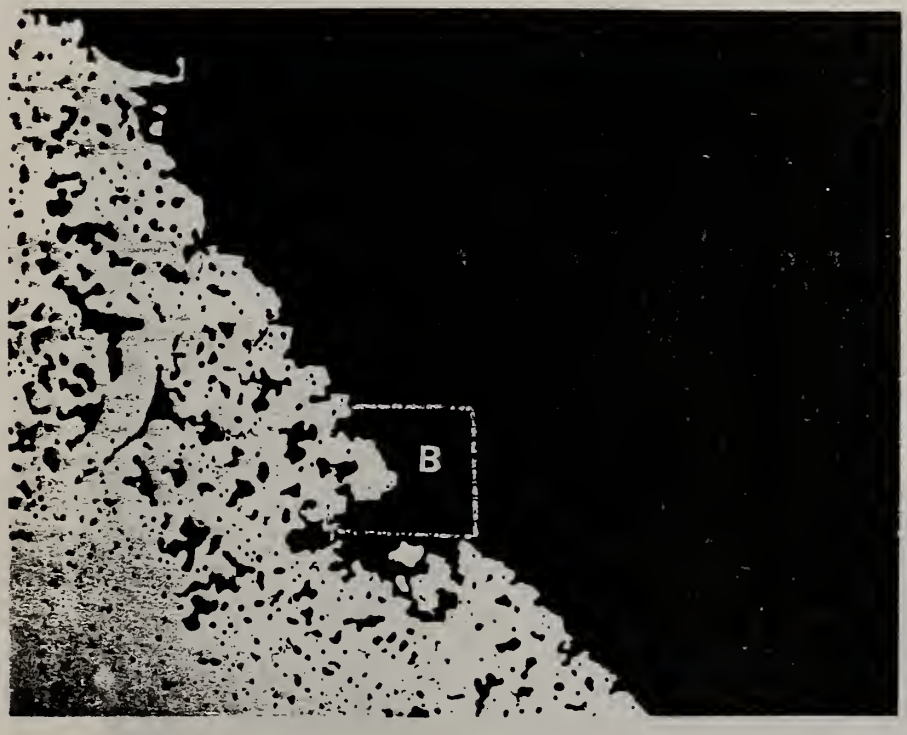

Figure 3. SEM micrograph showing area A of figure 2 at 100X.

Figure 4. SEM micrograph showing area B of figure 3 at 512X.

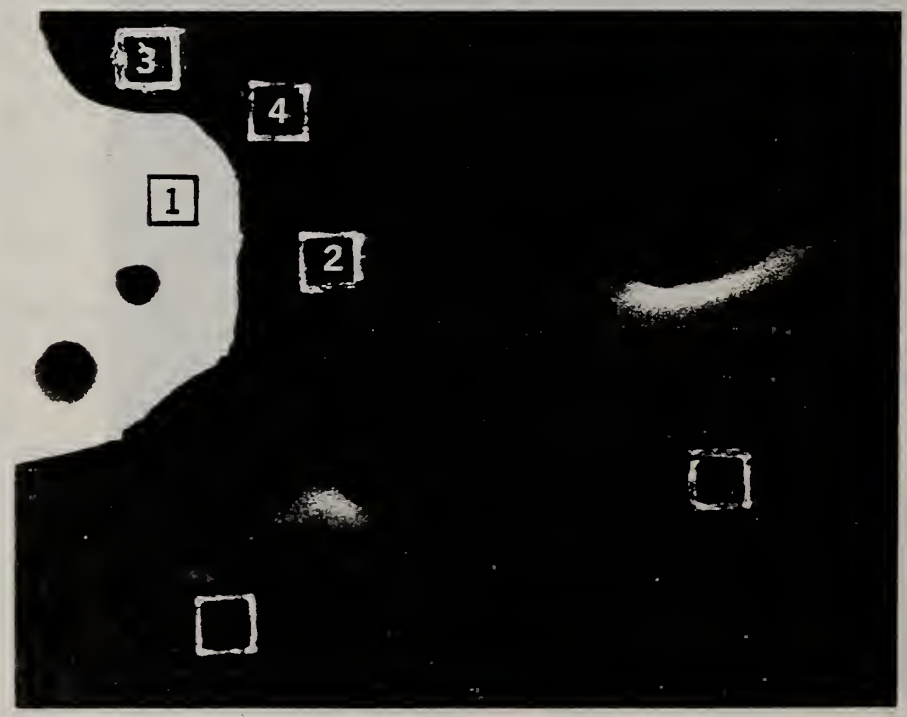

Figure 5. SEM micrograph showing area C of figure 4 at 2000X.

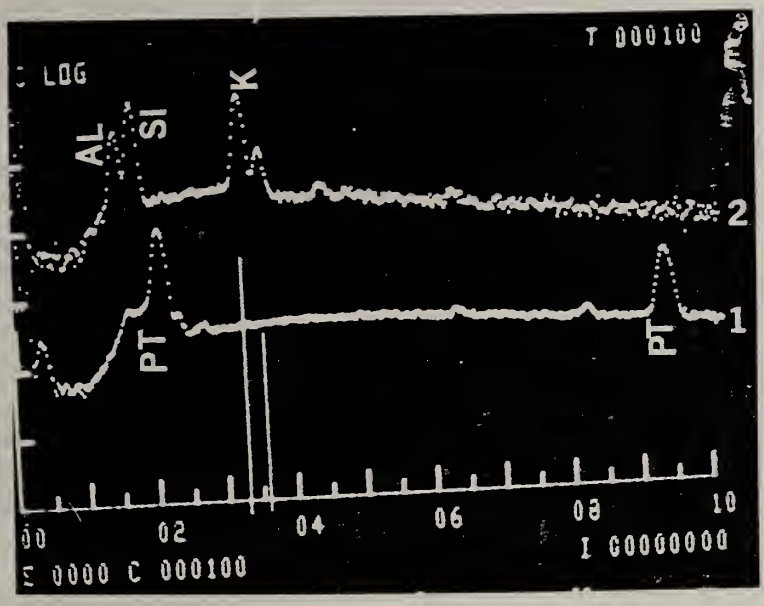

Figure 6a. EDAX spectra of areas 1 and 2 of figure 5.

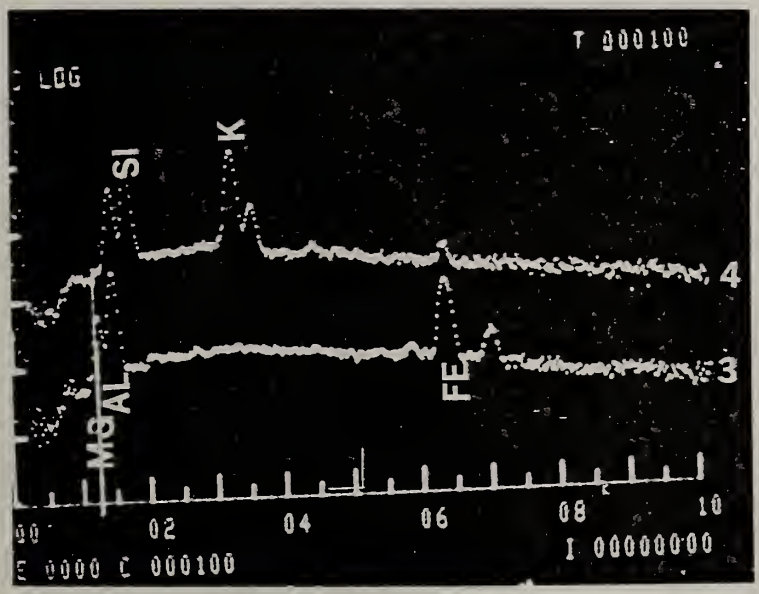

Figure 6b. EDAX spectra of areas 3 and 4 of figure 5.

3. Corrosion of Downstream MHD Components (J. Smit, 561 and C. D. Olson, 565)

Introduction: The efficient utilization of materials in a combined cycle magnetohydrodynamic (MHD) steam power electrical generating system requires a knowledge of the behavior of these materials to some or all of the characteristics of the working environment. A major component of large tonnage, and having a direct bearing on the efficiency of operation of the system is the heat exchanger in the steam bottoming plant. The materials in this unit must function for extended periods, years, in a corrosive and errosive milieu. A first step, a screening step, to determine the suitability of materials for this application entails the evaluation of these materials after brief exposure to some of the characteristics of the harsh environment expected. Selected specimens are therefore being exposed to fuel-rich and oxygen-rich, metal salt-seeded, hot gas streams which reproduce some of these downstream conditions. Data from these exposure tests should give an indication, to a first approximation, of the potential suitability for service of these materials.

Progress: The utilization of clad materials for application in downstream MHD components is an attractive alternative to conventional materials from both the standpoint of durability (corrosion reduction) and economics (reduction of consumption of scarce resources). Arc plasma-sprayed coatings, one such class of clad materials, has recently generated much interest. As a consequence attention is now being given to the testing and evaluation of three commercially available examples of this type of coating. Specimens of these coatings, NiCrAlY, $MgAl_2O_4$ (spinel) and ZrO_2 (doped with MgO) have been obtained, and arc plasma-sprayed on mild steel (AISI 1015) tubing. The coating thickness averages 0.5 mm. Short length specimens of each, 75 mm long, were obtained for characterization prior to test and for thermal cycling tests. Longer specimens, 0.25 m in length, with Pt/Pt-10% Rh thermocouples welded into the mid points (prior to arc plasma spraying) were obtained for corrosion testing. All tubing is 12.7 mm in diameter with a wall thickness of 1.6 mm.

Sections of the 75 mm long specimens were examined in the as-received condition, after cycling to 700 °C in air and after cycling to 700 °C in forming gas (5% H_2, 95% N_2). During these cycles the specimens were held at the peak temperature for about 36 hours. Heat up and cool down rate was approximately 3°/min. Cross sections were prepared using standard metallographic techniques. The examination was conducted using SEM-EDX techniques.

A. Characterization of NiCrAlY: The composition of the NiCrAlY coating is nominally 20% Cr, 12% Al, 1/10% Y with the remainder Ni (wt.%). Figures 1, 2, and 3 are sections of the NiCrAlY in the as received condition showing the bonding to the AISI 1015 mild steel tubing and the apparent lack of homogeneity of the sprayed coating. This is confirmed by the species maps, Figs. 4, 5, and 6, which show in detail the distribution of the species associated with Fig. 3. Note what appear to be islands of chromium in a matrix of nickel.

Thermal cycling in air and in forming gas had no discernable effect on the NiCrAlY specimens. Figures 7, 8, and 9 show the species distribution associated with Fig. 10 (specimen cycled in air). Figures 11 and 12 show the species distribution associated with Fig. 13 (specimen cycled in forming gas). It was noted that some iron contamination existed in all sections examined. The source of this is unknown at this time.

The NiCrAlY surface is shown in Figs. 14, 15, and 16. It appears at low magnification to be quite pocked, Fig. 14. At higher magnification, Figs. 15 and 16, the surface appears to be covered with platelets. These platelets also appear to contain micropores. This surface roughness accompanied with inhomogeneity of the species may ultimately pose a corrosion problem as crevices in the surface may promote corrosion and the increase in real surface area with respect to the apparent area may enhance it.

B. Characterization of $MgAl_2O_4$: The $MgAl_2O_4$ is bonded to the mild steel through a graded NiCrAlY coating which is nominally 0.1 mm thick. The NiCrAlY shows the same characteristic inhomogeneity as described earlier. In the as received condition the bond between the $MgAl_2O_4$ and the NiCrAlY appears everywhere to be intact as does the bond between the NiCrAlY and the mild steel, Fig. 17. $MgAl_2O_4$ also appears to be uniform and continuous, Fig. 18. Thermal cycling in forming gas had no effect on the coherency of the coating but did result in the formation of voids, Figs. 19 and 20, while cycling in air resulted in cracking parallel to the substrate surface, but, interestingly just above the NiCrAlY bond coat and not at the interface itself, Figures 21 and 22. Note also the porosity. Calcium contamination was also observed. The surface, as received,is also pocked and appears to be covered with platelet-type forms, Fig. 23 and 24.

C. Characterization of ZrO_2 (doped): The MgO doped ZrO_2 is bonded to the mild steel substrate in a manner similar to that described for the $MgAl_2O_4$. As received the ZrO_2 appears to be well bonded to the intermediate NiCrAlY coat which in turn is well bonded to the mild steel substrate. The coating itself however contains regions of large voids paralleling the substrate surface, Figs. 25 and 26. No adverse effects resulted from thermal cycling in forming gas. Regions of voids, Figs. 27 and 28 exist in this specimen similar to that in the as received condition. Thermal cycling in air resulted in cracking parallel to the substrate surface and cracking normal to the surface, Figs. 29 and 30. Note that cracking here occurred at the ZrO_2-NiCrAlY interface. Some Fe contamination was observed throughout the ZrO_2 coating.

At low magnification, the surface of the as received material appears pocked, Fig. 31. At higher magnification, microcracks are evident, Fig. 32.

D. Examination of AISI 1015 Steel: AISI 1015 steel tubing, the material used as a substrate for the arc plasma-sprayed coating, was, in addition, exposed to oxygen rich and fuel rich K_2SO_4 seeded hot gas streams. The tubing, 12.7 mm in diameter with a wall thickness of 1.6 mm, was prepared in 0.25 m lengths with Pt/Pt 10% Rh thermocouples welded into the midpoint position. Prior to exposure the specimens were cleaned to constant weight in an ultrasonic bath at 50 °C in a 10% by weight ammonium citrate solution.

The specimens were exposed for four hours,exclusive of heat up and cool down time. In the vicinity of the specimen the gas stream temperature was maintained at approximately 1300 °C. Tube wall temperature was held at 590 °C. The gas stream was seeded with K_2SO_4 for 25 minutes at the start of the four hour interval at a rate of 25 gm/min. Immediately after cool down the specimens were encapsulated and subsequently sectioned, ground, and polished using standard metallographic techniques with the exception that at all stages

nonaqueous cutting and cooling media were used to prevent the occurrence of post exposure reactions.

The AISI 1015 specimen, exposed at 590 °C to the oxygen rich K_2SO_4 seeded hot gas stream, developed a very adherent K_2SO_4 corrosion product coating with no lifting of the entire coating evident, i.e., no indication of epoxy between the tubing and the corrosion coating. Figure 33 shows this adhesion on the top (leading surface) region of the tube. Higher magnification, Fig. 34, reveals what appears to be cracking at the surface. Figure 35, at still higher magnification shows this cracking to occur as scaling in the top portion of the steel. EDX analysis, Figs. 36-40, show potassium penetration under the scale. The potassium readily reacts with iron, forming K + Fe products in this region. Sulfur on the other hand does not react as easily and is found in high concentration at the upper surface of the scale where Fe + S products are being formed. The general formation zones in the corrosion reaction region, from the tubing outward, is as follows: (a) AISI 1015 steel; (b) K + Fe reaction zone; (c) scale layer, K + Fe; (d) K + Fe + high S reaction zone; and (e) S + K + trace Fe, outer reaction band. This pattern is apparent over the entire surface of the tube with the reaction being most severe on the leading surface under the columnar salt deposit and least under the powdery fume deposit. The corrosion band thickness ranges from about 35 mm at the leading surface (under the columnar deposit) to about 20 μm under the fume deposit.

A similarly adherent salt-corrosion product coating formed on the AISI 1015 steel specimen exposed at 590 °C to a fuel rich K_2SO_4 seeded hot gas stream. Again, no general lifting was observed. Figure 41 shows the corrosion zone on the leading surface (tube top). This area is not as extensive as seen under oxygen rich conditions nor is there a separation in the scale. The area under the drop zone shows a similar corrosion response to the K_2SO_4 seed. Potassium is found throughout the corrosion zone as well as sulfur, Figs. 42-46. The products here being some combination of K, Fe, + S and Fe + S. It should be noted that the migration of Fe goes well into the salt coating beyond the corrosion band. Corrosion appears in this case to be more uniform over the entire circumference of the tube and ranges around 10 μm in thickness. The demonstrated susceptibility of AISI 1015 to attack from exposure to the conditions described emphasizes the importance of the structural integrity of whatever class of clad materials is applied to this or similar inexpensive substrates.

Plans: (1) Conduct further exposure tests on arc plasma sprayed mild steel tubing. (2) Analyze and evaluate exposed arc plasma sprayed mild steel tubing using SEM/EDX techniques.

Fig. 1 Optical micrograph of a section of arc plasma-sprayed NiCrAlY steel.

Fig. 2 SEM micrograph, 50x, showing in detail the bonding of the NiCrAlY coating to the AISI 1015 mild steel.

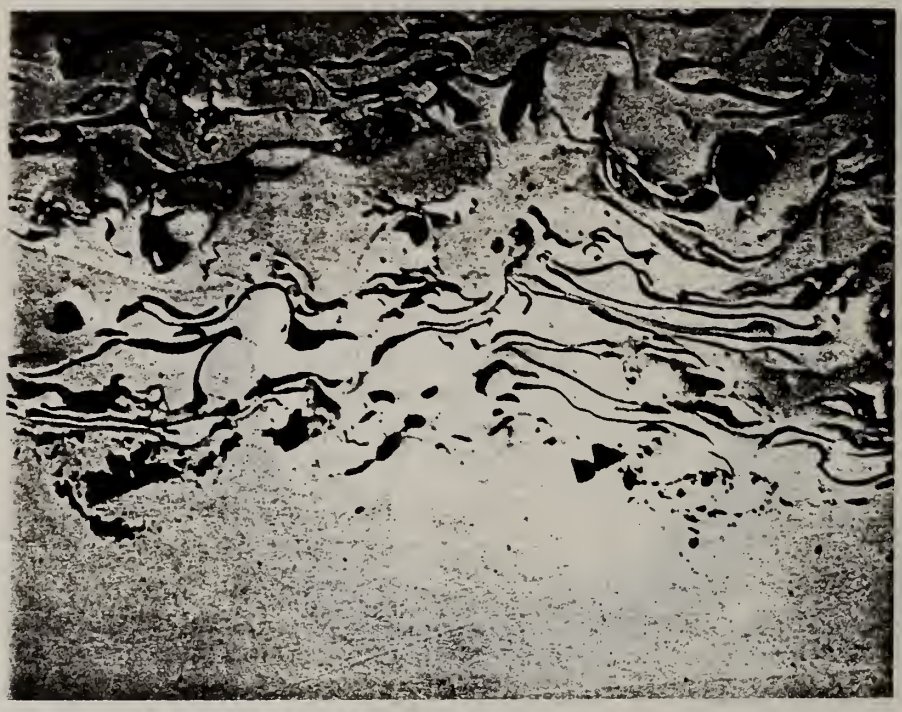

Fig. 3 SEM micrograph, 504x, of the mid region of Fig. 2, showing in detail the distribution of materials in the NiCrAlY coating as received.

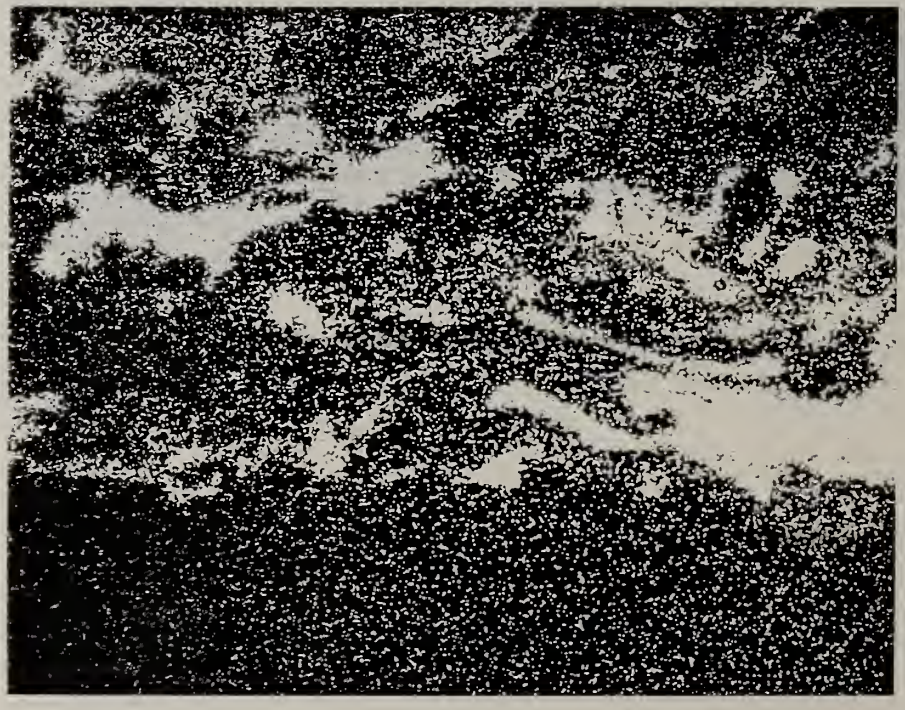

Fig. 4 EDX specie map of region shown in SEM micrograph Fig. 3 showing distribution of chromium

Fig. 5 EDX specie map of region shown in SEM micrograph Fig. 3 showing distribution of nickel.

Fig. 6 EDX specie map of region shown in SEM micrograph Fig. 3 showing distribution of iron at NiCrAlY- AISI 1015 interface.

Fig. 7 EDX specie map of region shown in SEM micrograph Fig. 10 showing distribution of nickel.

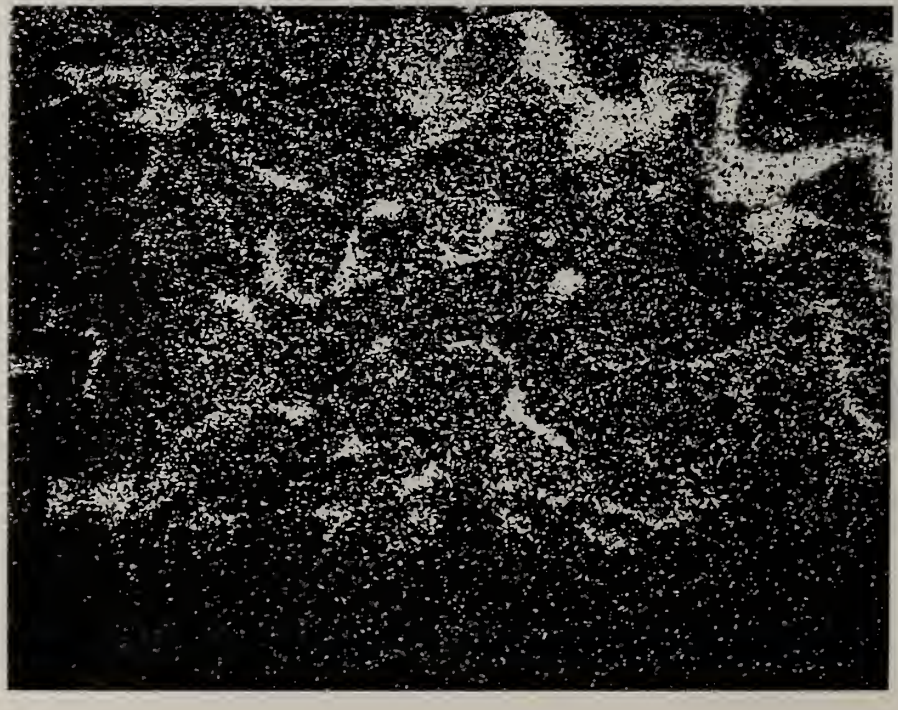

Fig. 8 EDX specie map of region shown in SEM micrograph Fig. 10 showing distribution of chromium.

Fig. 9 EDX specie map of region shown in SEM micrograph Fig. 10 showing distribution of aluminum.

Fig. 10 SEM micrograph, 464x, showing in detail the distribution of material in the NiCrAlY coating after cycling in air.

Fig. 11 EDX specie map of region shown in SEM micrograph Fig. 13 showing distribution of nickel.

Fig. 12 EDX specie map of region shown in SEM micrograph Fig. 13 showing distribution of chromium.

Fig. 13 SEM micrograph,476x, showing in detail the distribution of material in the NiCrAlY coating after cycling in forming gas.

Fig. 14 SEM micrograph, 22x,of NiCrAlY surface.

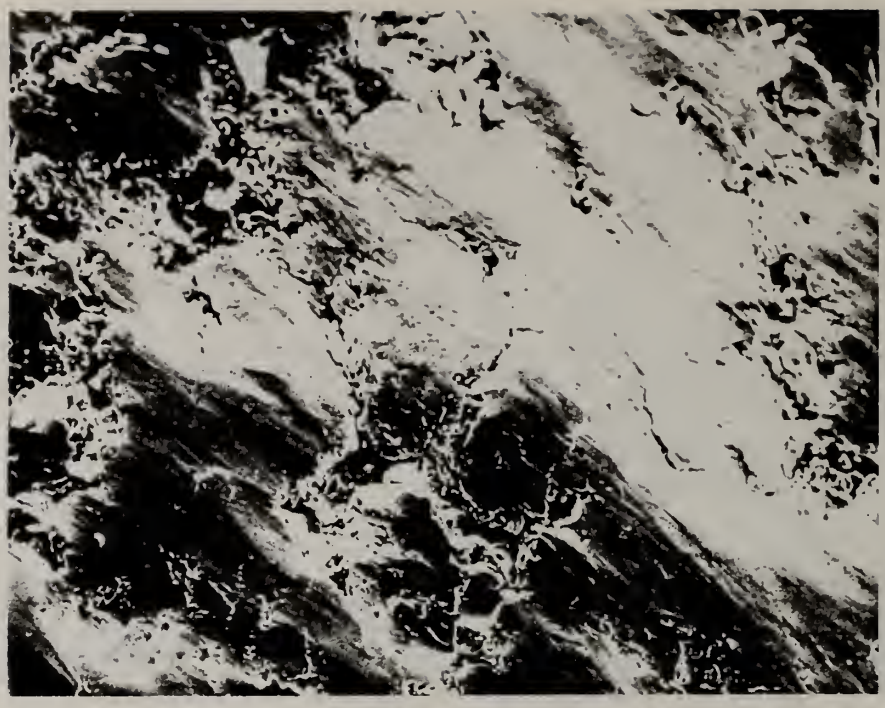

Fig. 15 SEM micrograph, 112x, of NiCrAlY surface.

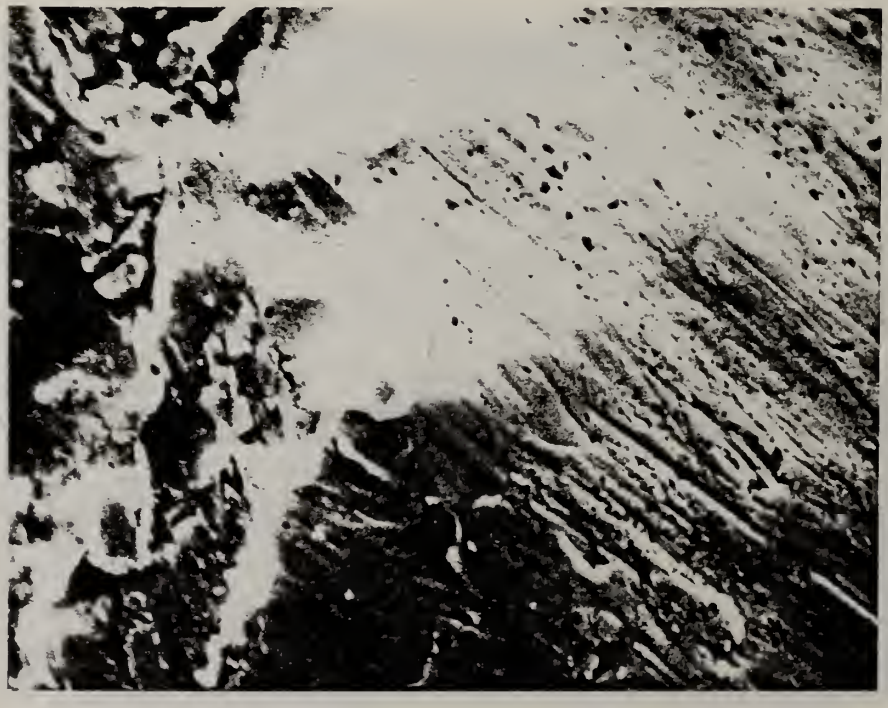

Fig. 16 SEM micrograph, 2240x, of NiCrAlY surface.

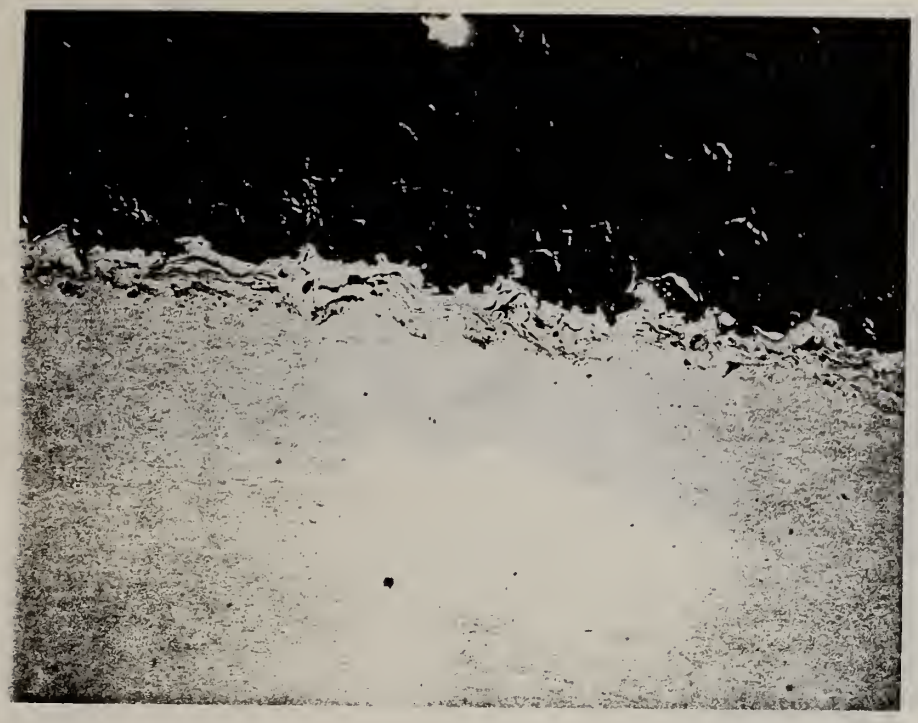

Fig. 17 SEM micrograph, 112x, of a section of arc plasma-sprayed $MgAl_2O_4$ coating on AISI 1015 steel showing graded bond.

Fig. 18 SEM micrograph, 112x, of arc-plasma-sprayed $MgAl_2O_4$ coating.

Fig. 19 SEM micrograph, 96x, of $MgAl_2O_4$ cycled in forming gas to 700°C, showing voids.

Fig. 20 SEM micrograph, 950x, of $MgAl_2O_4$ of mid region of Fig. 19.

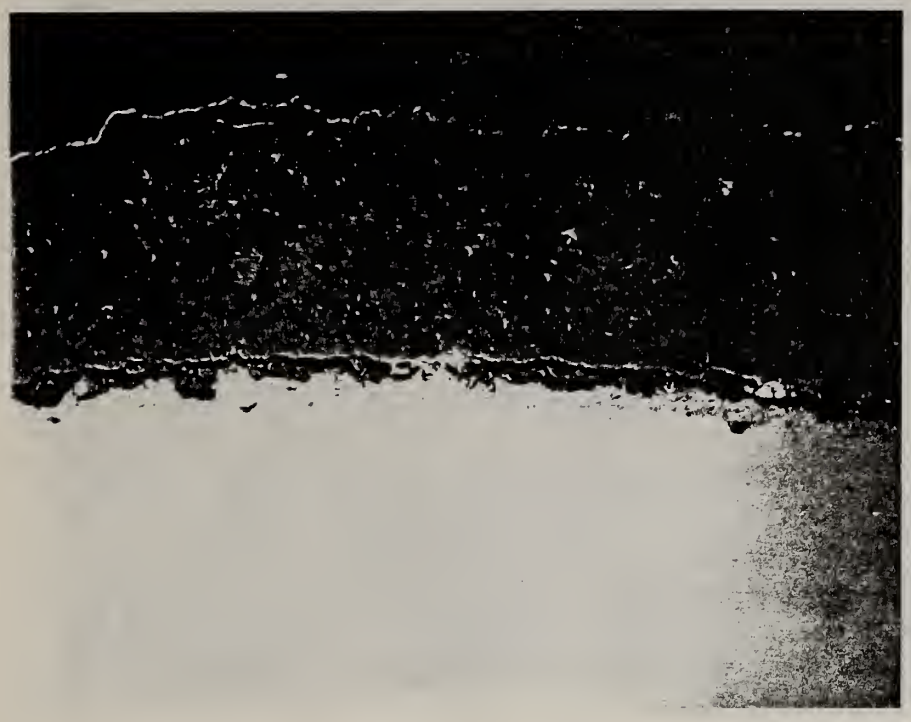

Fig. 21 SEM micrograph, 43x, of $MgAl_2O_4$ cycled in air to 700°C showing cracking within the coating.

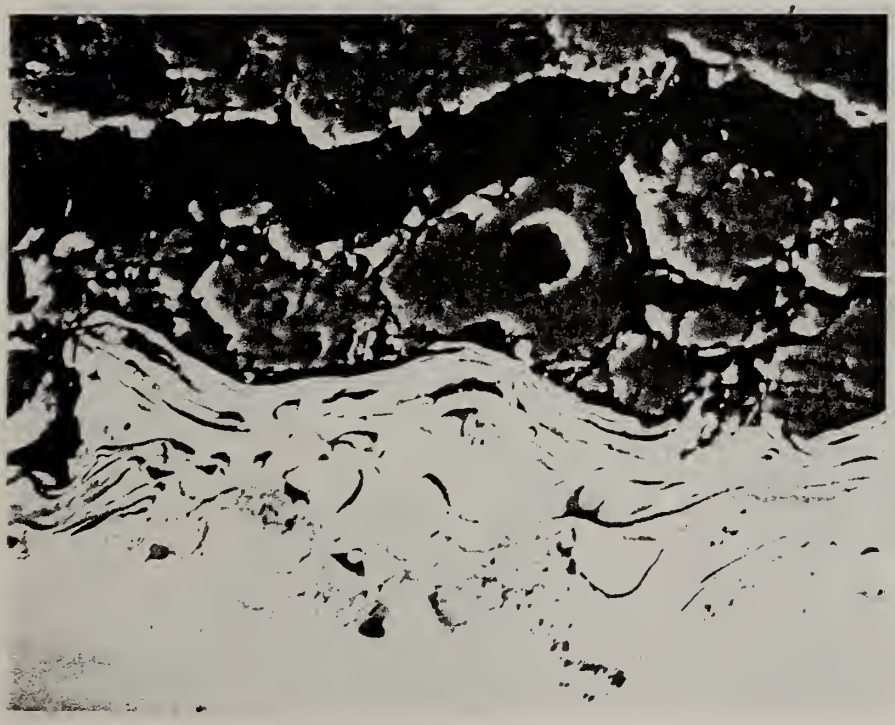

Fig. 22 SEM micrograph, 480x, of mid region of Fig. 21.

Fig. 23 SEM micrograph, 27x, of $MgAl_2O_4$ surface.

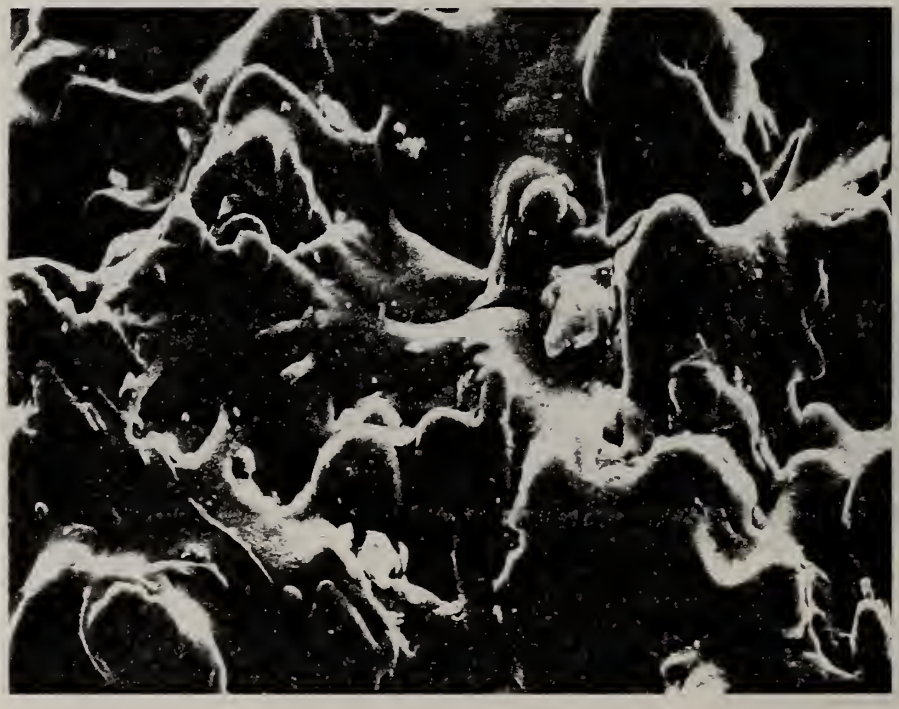

Fig. 24 SEM micrograph, 512x, of mid region of Fig. 23 showing platelet forms.

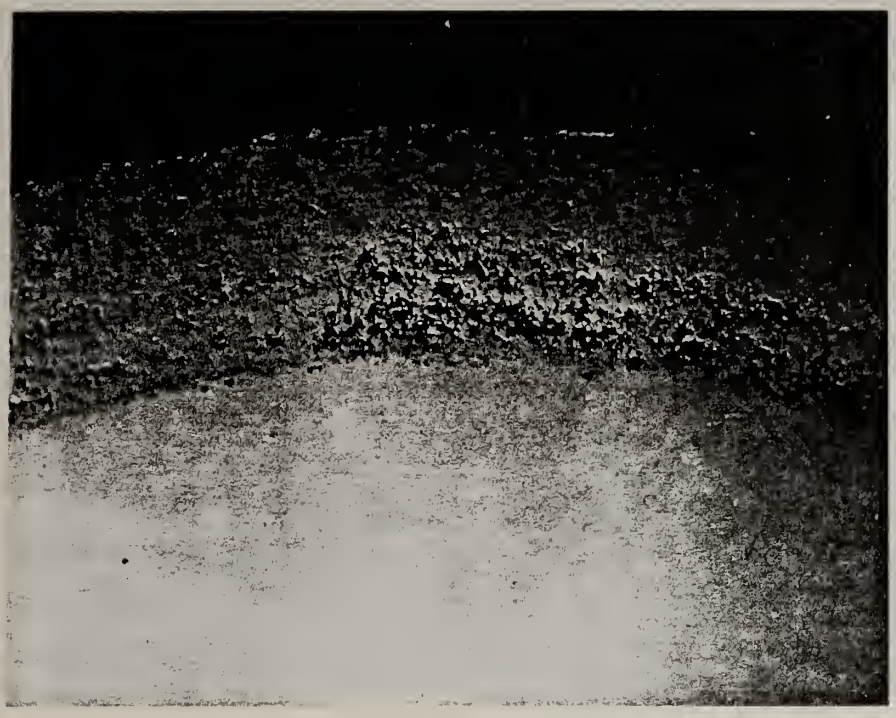

Fig. 25 SEM micrograph, 24x, of a section of arc plasma-sprayed doped ZrO_2 coating on AISI 1015 mild steel showing large void areas.

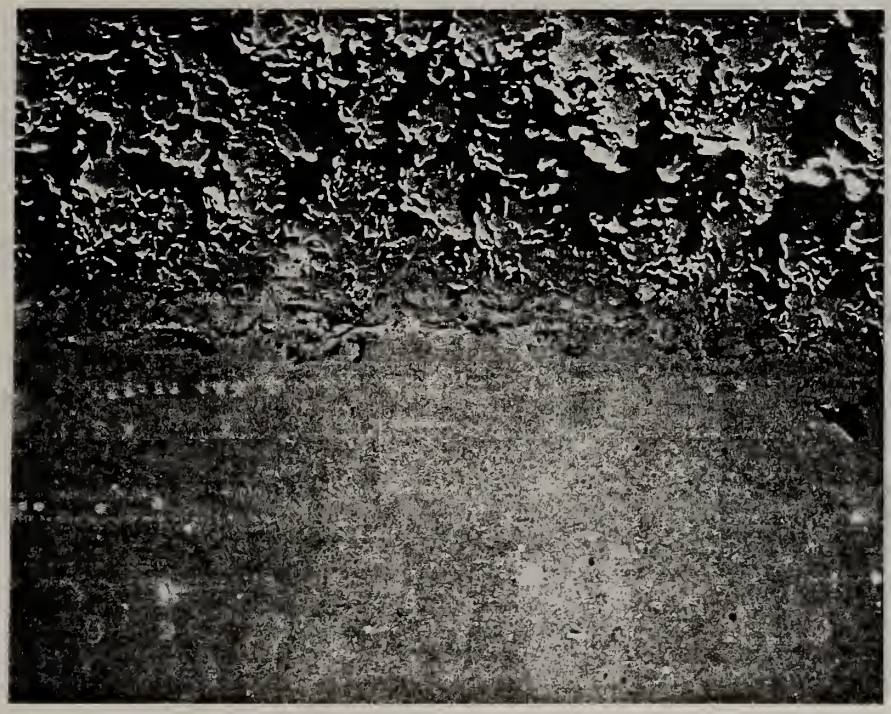

Fig. 26 SEM micrograph, 120x, of mid region of Fig. 25.

Fig. 27 SEM micrograph, 45x, of ZrO_2 after cycling in forming gas to 700°C showing voids.

Fig. 28 SEM micrograph, 180x, of mid region of Fig. 27.

Fig. 29 SEM micrograph, 50x, of ZrO_2 after cycling in air to 700°C showing cracks parallel and normal to the substrate tubing.

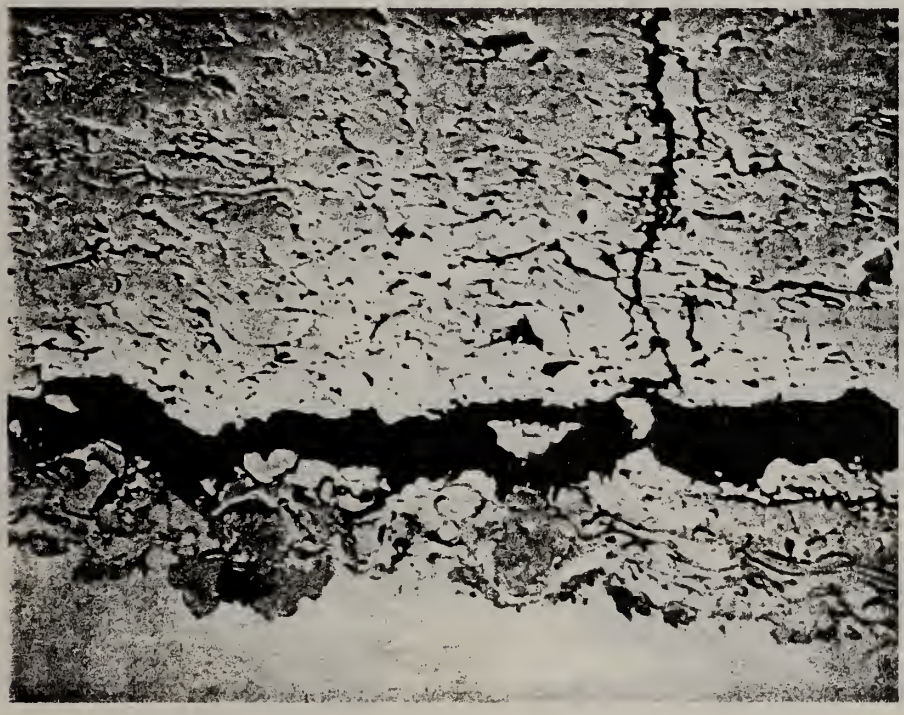

Fig. 30 SEM micrograph, 206x, of mid region of Fig. 29.

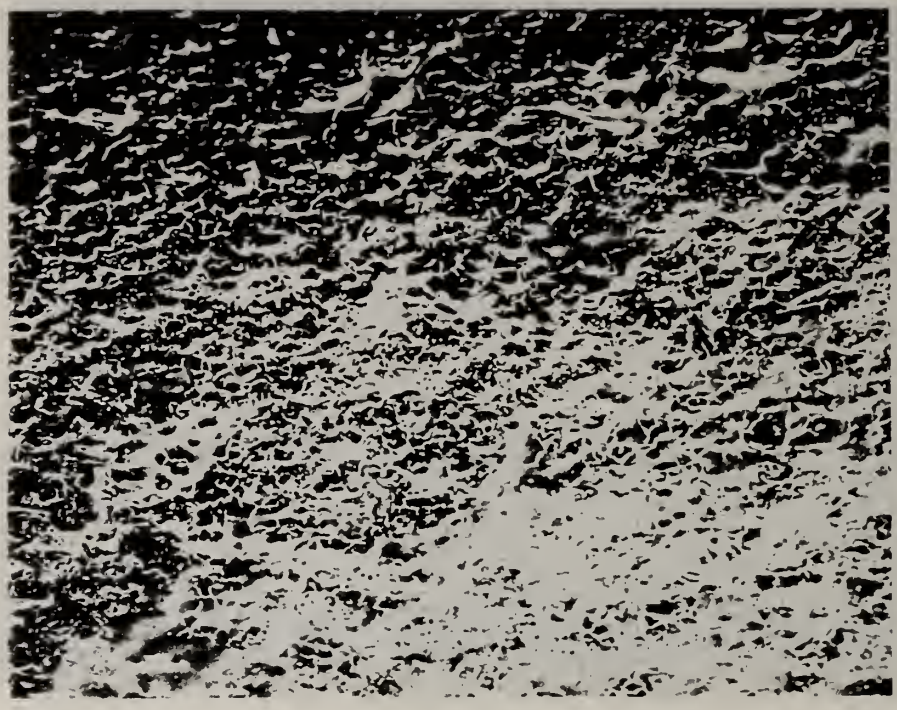

Fig. 31 SEM micrograph, 50x, of ZrO_2 surface.

Fig. 32 SEM micrograph, 206x, of mid region of Fig. 31 showing microcracks.

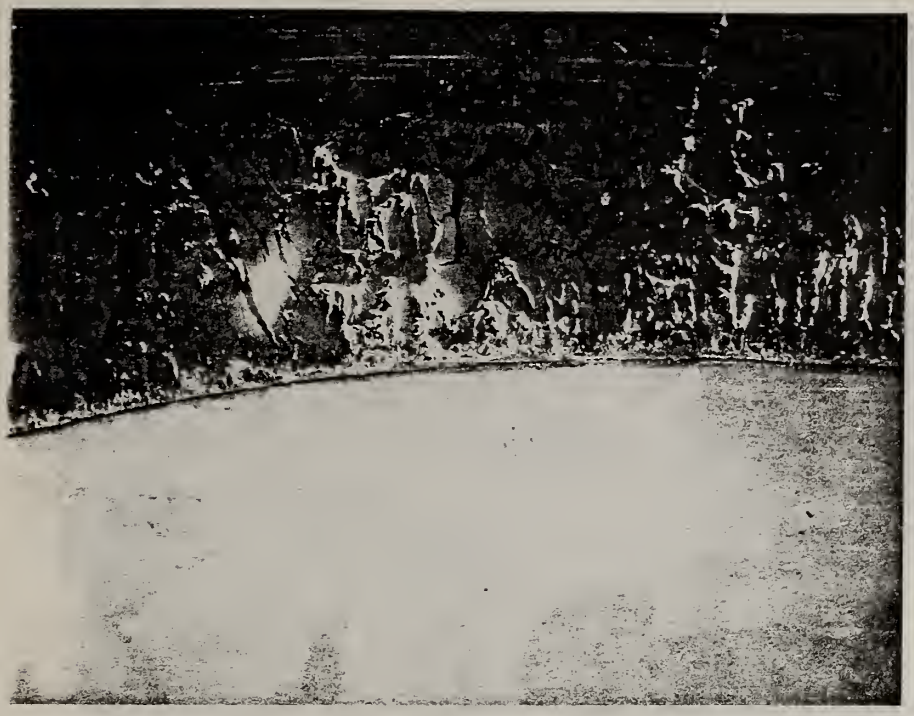

Fig. 33 SEM micrograph, 52x, of a section of AISI 1015 steel tubing after exposure to an oxygen-rich K_2SO_4-seeded hot gas stream. Surface shown faced the gas stream.

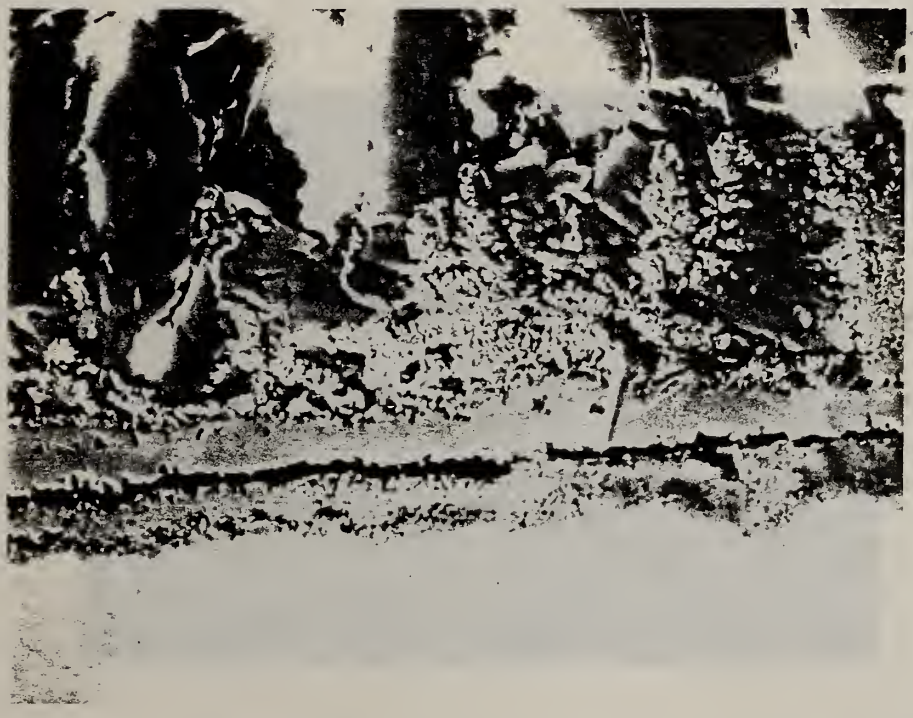

Fig. 34 SEM micrograph, 528x, of mid region of Fig. 33 showing scale.

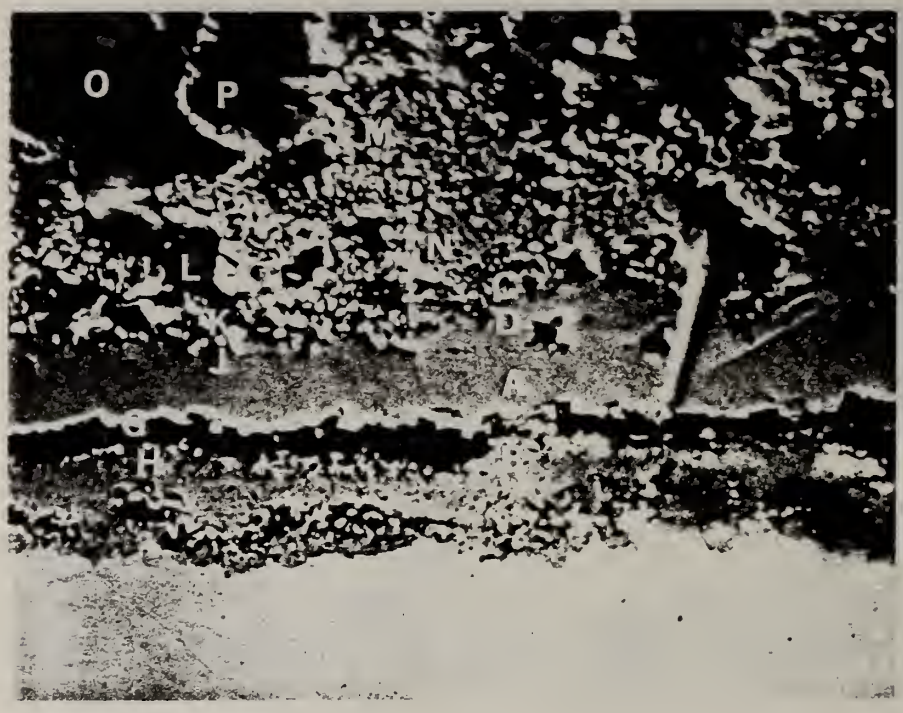

Fig. 35 SEM micrograph, 1080x, of mid region of Fig. 33 showing cracking in the scale. Lettered regions correspond to labeled EDX spectra Figs. 36-43.

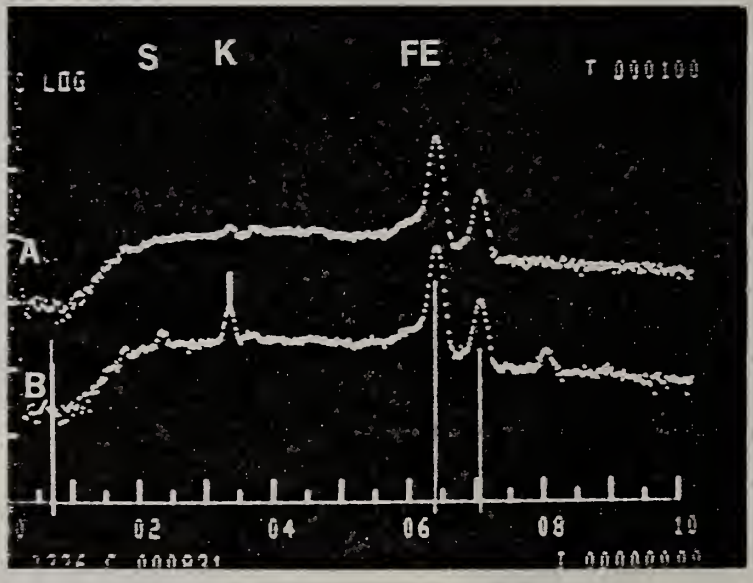

Fig. 36 EDX spectra of regions A and B of Fig. 35 showing iron across the scale break. Specie positions and designations of all spectra in this report are as indicated above.

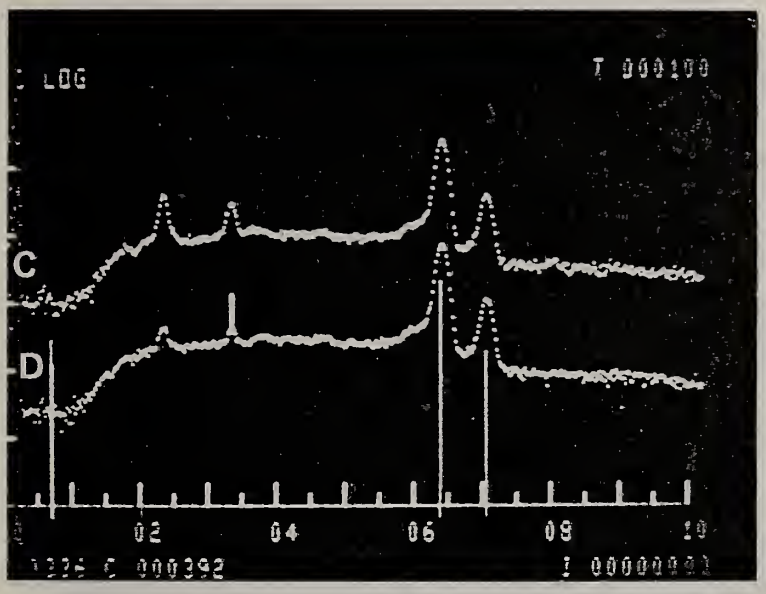

Fig. 37 EDX spectra of region C and D of Fig. 35 showing potassium sulfur and iron at scale-salt deposit interface.

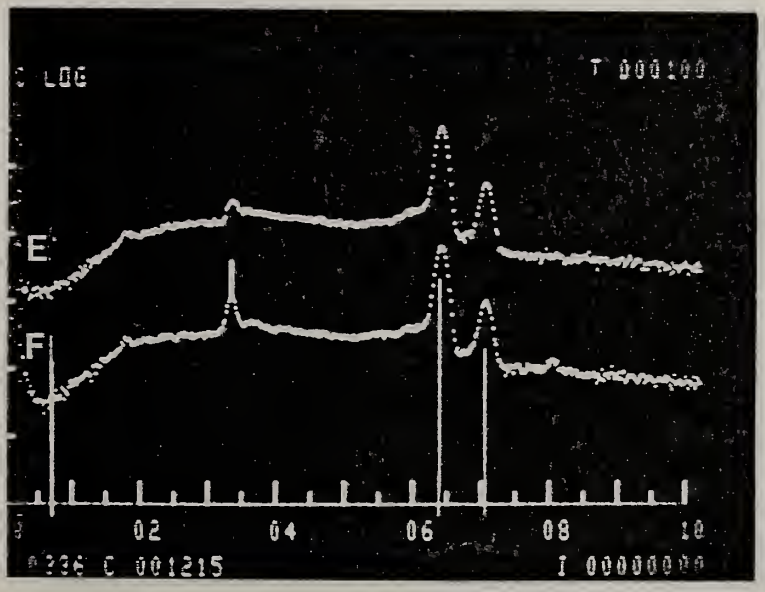

Fig. 38 EDX spectra of regions E and F of Fig. 35 showing potassium penetration into the AISI 1015 bulk steel.

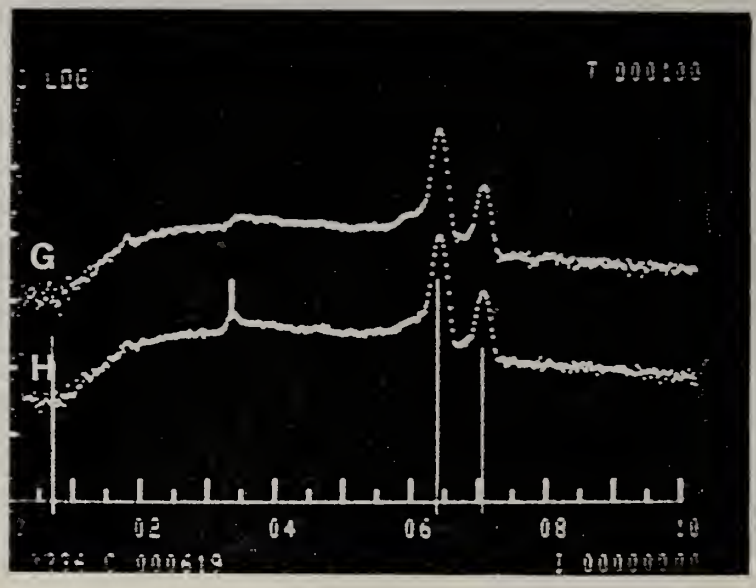

Fig. 39 EDX spectra of regions G and H of Fig. 35 showing iron at the scale crack.

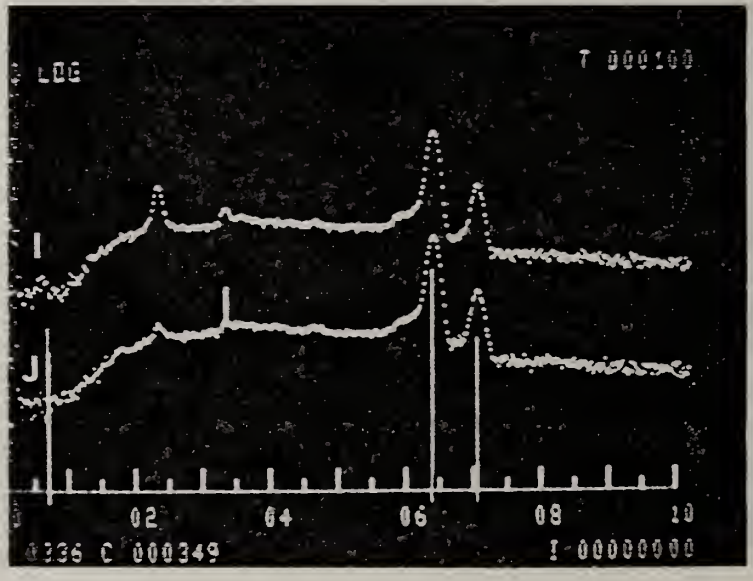

Fig. 40 EDX spectra of regions I and J of Fig. 35 showing iron, potassium and sulfur across scale-salt deposit interface.

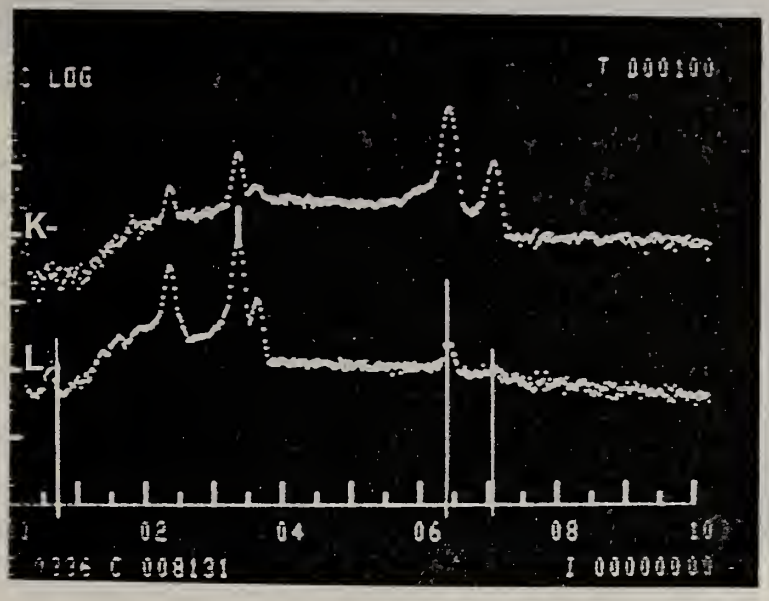

Fig. 41 EDX spectra of regions K and L of Fig. 35 showing iron penetration into the salt coating.

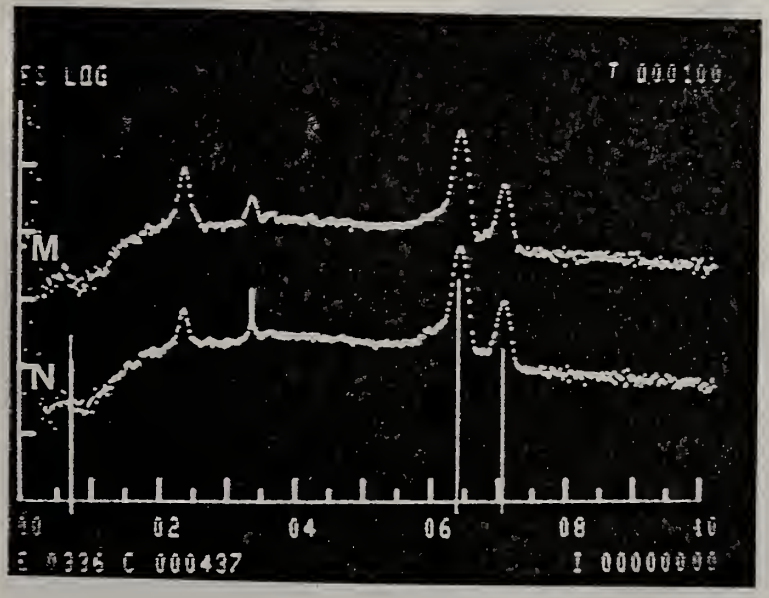

Fig. 42 EDX spectra of regions M and N of Fig. 35 showing iron penetration into the salt coating.

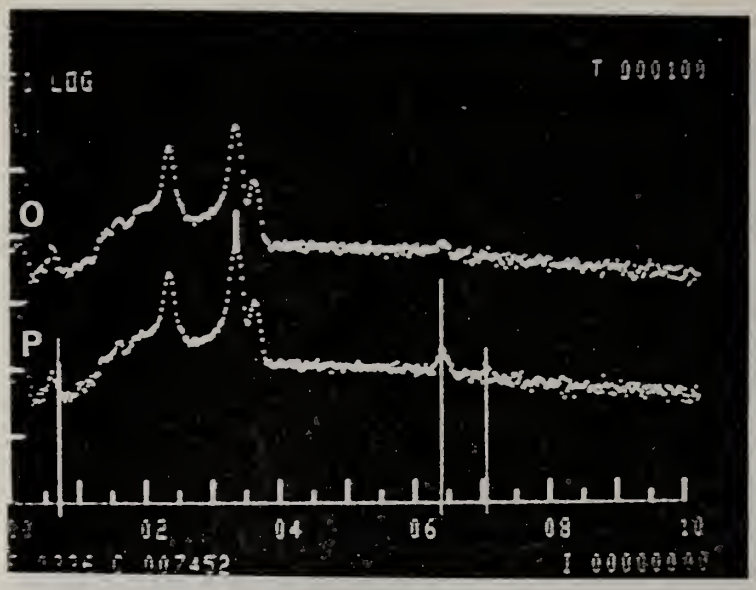

Fig. 43 EDX spectra of regions O and P of Fig. 35 showing farthest penetration of iron into the salt coating.

Fig. 44 SEM micrograph, 920x, of a section of AISI 1015 steel tubing after exposure to a fuel-rich, K_2SO_4-seeded hot gas stream. Surface shown faced the gas stream.

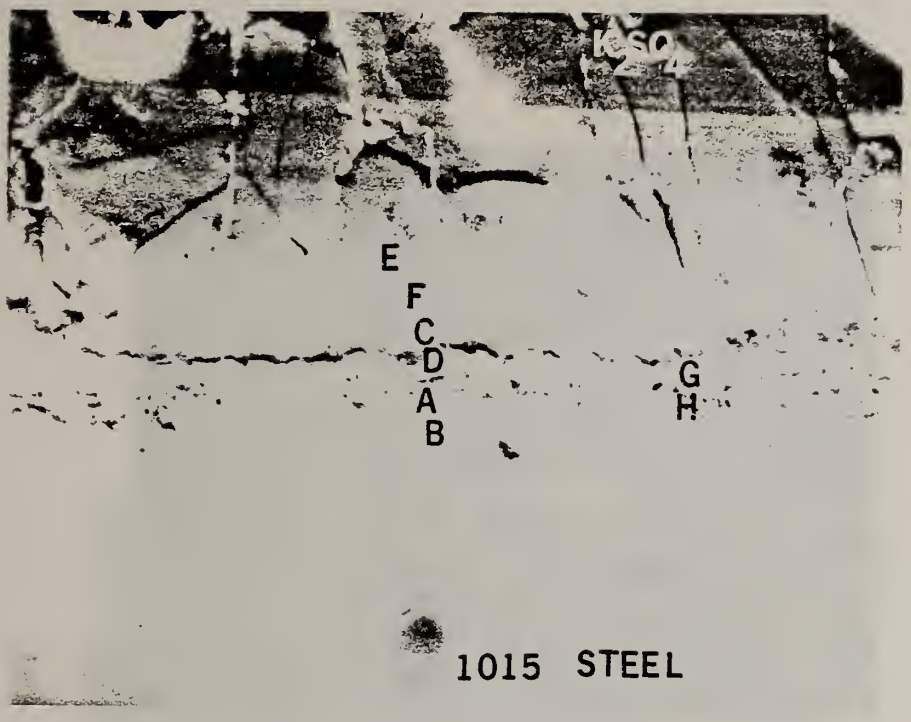

Fig. 45 SEM micrograph, 920x, of surface of tube of Fig. 44 showing corrosion at side of tube. Lettered regions correspond to labeled EDX spectra Figs. 46-49.

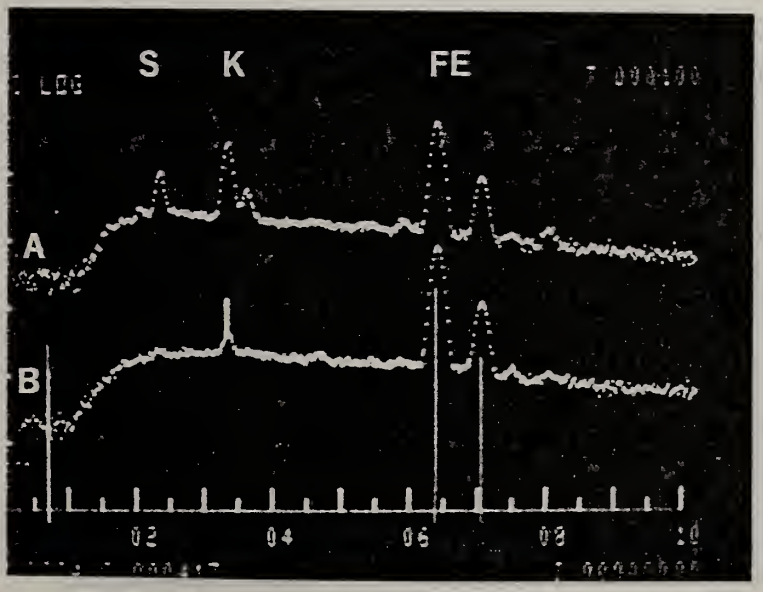

Fig. 46 EDX spectra of regions A and B of Fig. 45 showing potassium and sulfur penetration at bulk AISI 1015-corrosion band interface.

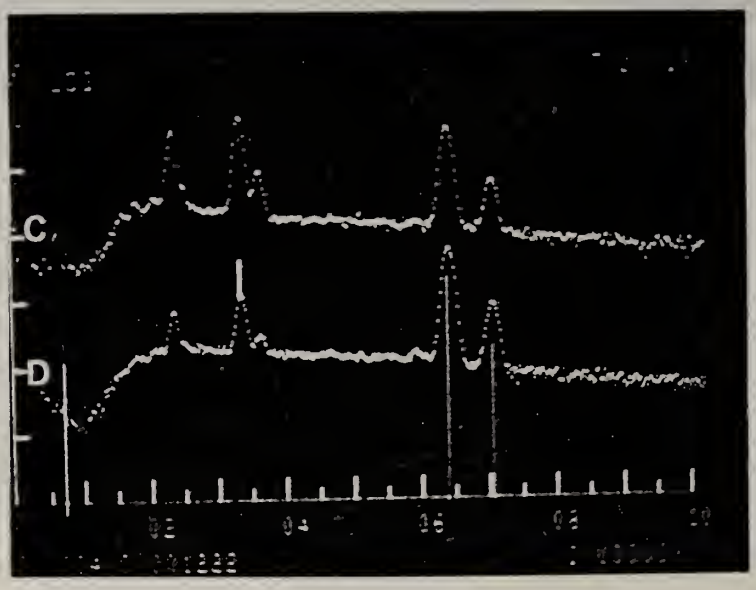

Fig. 47 EDX spectra of regions C and D of Fig. 45 showing high iron peak comparableto the bulk at the corrosion band-salt coating interface.

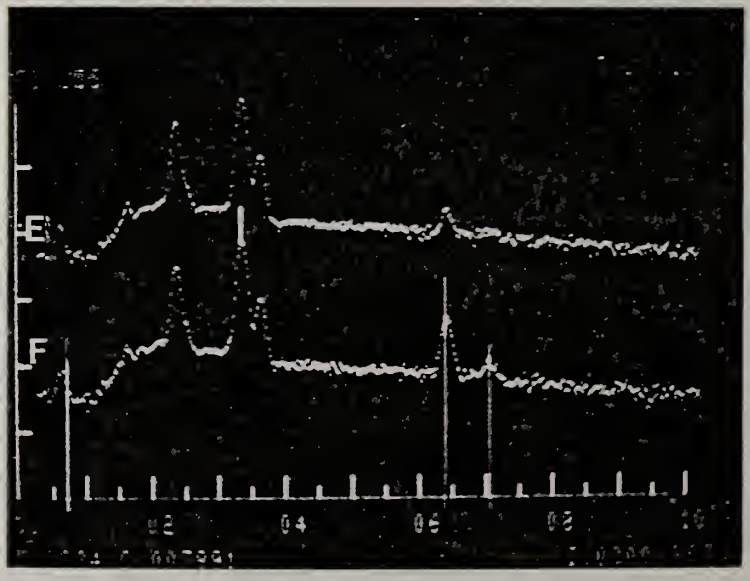

Fig. 48 EDX spectra of regions E and F of Fig. 45 showing iron penetration into the salt coating.

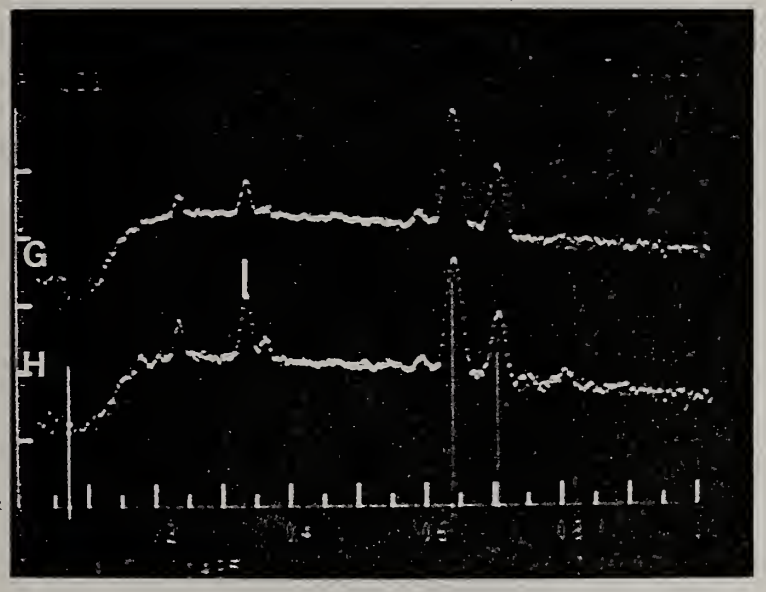

Fig. 49 EDX spectra of regions G and H of Fig. 45 showing potassium and sulfur penetration in another region of the corrosion band.